HHS Public Access

Author manuscript

Nat Neurosci. Author manuscript; available in PMC 2024 May 19.

Published in final edited form as:

Nat Neurosci. 2024 May ; 27(5): 873–885. doi:10.1038/s41593-024-01610-w.

TREM1 disrupts myeloid bioenergetics and cognitive function in aging and Alzheimer's disease mouse models

Edward N. Wilson[1,2], **Congcong Wang**[1], **Michelle S. Swarovski**[1], **Kristy A. Zera**[1], **Hannah E. Ennerfelt**[1], **Qian Wang**[1], **Aisling Chaney**[1,5], **Esha Gauba**[1], **Javier A. Ramos Benitez**[1], **Yann Le Guen**[1], **Paras S. Minhas**[1], **Maharshi Panchal**[1], **Yuting J. Tan**[1], **Eran Blacher**[1], **Chinyere A. Iweka**[1], **Haley Cropper**[1,5], **Poorva Jain**[1,5], **Qingkun Liu**[1], **Swapnil S. Mehta**[1], **Abigail J. Zuckerman**[1], **Matthew Xin**[1], **Jacob Umans**[1], **Jolie Huang**[1], **Aarooran S. Durairaj**[1], **Geidy E. Serrano**[6], **Thomas G. Beach**[6], **Michael D. Greicius**[1,2], **Michelle L. James**[1,2,5], **Marion S. Buckwalter**[1,2,7], **Melanie R. McReynolds**[3,4,8], **Joshua D. Rabinowitz**[3,4], **Katrin I. Andreasson**[1,2,9,*]

[1]Dept of Neurology & Neurological Sciences, Stanford University School of Medicine, Stanford, CA, 94305, USA

[2]Wu Tsai Neurosciences Institute, Stanford University, Stanford, CA, USA

[3]Lewis-Sigler Institute for Integrative Genomics, Princeton University, Princeton, NJ, USA

[4]Dept of Chemistry, Princeton University, Princeton, NJ, USA

[5]Dept of Radiology, Stanford University School of Medicine, Stanford, CA, 94305, USA

[6]Civin Laboratory for Neuropathology, Banner Sun Health Research Institute, Sun City, AZ 85351, USA

[7]Dept of Neurosurgery, Stanford University School of Medicine, Stanford, CA, USA

[8]Dept of Biochemistry and Molecular Biology, Huck Institutes of the Life Sciences, Pennsylvania State University, University Park, PA 16802

[9]Chan Zuckerberg Biohub, San Francisco, CA 94158

Abstract

Human genetics implicate defective myeloid responses in the development of late onset Alzheimer's disease (AD). A decline in peripheral and brain myeloid metabolism, triggering maladaptive immune responses, is a feature of aging. The role of TREM1, a pro-inflammatory factor, in neurodegenerative diseases is unclear. Here, we show that Trem1 deficiency prevents

*Correspondence should be addressed to: kandreas@stanford.edu.

AUTHOR CONTRIBUTIONS

E.N.W. and K.I.A. conceived and planned this study. E.N.W., T.G.B., M.D.G., M.L.J., M.S.B, J.D.R. and K.I.A contributed to supervising experimental design. E.N.W., C.W., H.E.E., M.S.S., M.R.M., Q.W., K.A.Z., A.C., J.A.R.B., E.G., P.S.M., E.B., Y.J.T., C.A.I., Y.L.G., M.P., H.C., P.J., Q.L., S.S.M., A.J.Z., M.X., J.U., J.H., A.S.D. and G.E.S. conducted the experiments. E.N.W., C.W., H.E., M.S.S., A.C., J.A.R.B., E.G., P.S.M., Y.L.G., A.J.Z. M.X., J.U., and J.H. performed collection of the data and statistical analysis. E.N.W. and K.I.A. wrote the manuscript. All authors reviewed and approved of the manuscript.

COMPETING FINANCIAL INTRESTS STATEMENT

M.L.J and K.I.A are co-founders and Scientific Advisory Board members of Willow Neuroscience, Inc. The remaining authors declare no competing interests.

age-dependent changes in myeloid metabolism, inflammation, and hippocampal memory function in mice. Trem1 deficiency rescues age-associated declines in ribose-5P. In vitro, Trem1 deficient microglia are resistant to amyloid-ß$_{42}$ oligomer (Aß$_{42}$)-induced bioenergetic changes, suggesting that Aß$_{42}$ stimulation disrupts homeostatic microglial metabolism and immune function via TREM1. In the 5XFAD mouse model, Trem1 haploinsufficiency prevents spatial memory loss, preserves homeostatic microglial morphology, and reduces neuritic dystrophy and changes in the disease-associated microglial transcriptomic signature. In aging APPSwe mice, Trem1 deficiency prevents hippocampal memory decline while restoring synaptic mitochondrial function and cerebral glucose uptake. In post-mortem AD brain, TREM1 colocalizes with Iba1+ cells around amyloid plaques and its expression is associated with AD clinical and neuropathological severity. Our results suggest that TREM1 promotes cognitive decline in aging and in the context of amyloid pathology.

Aging is the major risk factor for Alzheimer's disease (AD)[1,2] and is characterized by the development of persistent maladaptive inflammation[3,4]. Genome-wide association studies (GWAS) have identified genetic loci that associate with increased risk of AD[5], many of which contain genes expressed in myeloid cells, including brain microglia and peripheral monocytes and macrophages. This preponderance of myeloid genes suggests a pathogenic role for disrupted innate immunity in development of AD. Preclinical studies in mouse models of aging and AD pathology demonstrate that healthy microglial function is lost with advancing age and suggest that disease-modifying components of the innate immune response could be targeted to slow or halt disease progression. A well-studied myeloid receptor associated with AD is TREM2 (Triggering Receptor Expressed on Myeloid cells-2) where loss of function variants increase risk for AD[6–8]. TREM2 is an innate immune receptor that elicits anti- as well as pro-inflammatory responses and promotes Aβ clearance[9,10] and microglial survival[11]. In models of amyloid accumulation, microglia lacking *Trem2* or harboring the R47H *Trem2* variant show deficient proliferation, survival, clustering, phagocytosis, and Aβ plaque compaction[12–15].

The function of the family member TREM1 (Triggering Receptor Expressed on Myeloid cells-1) is distinct from that of TREM2. In sharp contrast, TREM1 amplifies pro-inflammatory innate immune responses to sterile damage associated molecular patterns (DAMPs) and infectious pathogenic molecular patterns (PAMPs)[16–21] (Fig. 1A). TREM1 synergizes with pattern recognition receptors such as toll-like receptors (TLRs) and NOD-like receptors (NLRs) to increase production of pro-inflammatory cytokines, proteases, and reactive oxygen species (ROS)[22–26]. Although TREM1 has not been identified in GWAS, targeted analysis of the *TREM1* locus has revealed an intronic variant of *TREM1* that is associated with increased amyloid load and rate of cognitive decline[27,28]. Given the pro-inflammatory function of TREM1 and its predominant expression on myeloid cells, we hypothesized that TREM1, in contrast to TREM2, may be involved in promoting age-associated, detrimental innate immune responses that are relevant to development of AD.

Recent studies indicate that myeloid cells, including peripheral monocytes, macrophages (MF) and brain microglia, undergo significant bioenergetic decline with aging[29–31], resulting in loss of beneficial immune responses, including the capacity to resolve

inflammation, clear pathogenic substances, and promote a homeostatic anti-inflammatory milieu. Here we report that TREM1 signaling disrupts myeloid cell metabolism and homeostatic immune responses in the contexts of both aging and brain amyloid accumulation, the two major risk factors for development of AD. We find that TREM1 deficiency restores youthful cellular metabolism and immune function to aging myeloid cells and prevents development of age-associated maladaptive inflammation and hippocampal memory decline in models of aging and AD.

TREM1 promotes cognitive decline via the periphery

Given that aging is a primary risk factor for development of AD, we first investigated whether TREM1 regulated cognitive aging. TREM1 was robustly expressed in peripheral $CD45^{+}CD11b^{+}$ myeloid cells in both blood and spleen, but at very low levels in brain microglia (Extended Data Fig. 1; Fig. 1b). With aging, TREM1 levels increased in blood (mean 40.96%) and brain (mean 3.63%). Ex vivo studies of wild type (WT) and *Trem1*−/− peritoneal macrophages (MF) confirmed that loss of TREM1 did not alter basal production of immune factors or phagocytosis but significantly dampened the immune response to lipopolysaccharide (LPS) stimulation (Extended Data Fig. 2). In vivo, age-associated changes in plasma immune factors, both pro- and antiinflammatory, were restored to youthful levels in aged $Trem1^{-/-}$ mice (Fig. 1c), as were anti-inflammatory CD71 and pro-inflammatory MHCII and CD86 surface markers in aged $Ly6C^{lo}$ MΦ (Fig. 1d; Extended Data Fig. 3a–c). In brain, age-associated increases in chemokines and cytokines also reverted to youthful levels in aged $Trem1^{-/-}$ cerebral cortex (Fig. 1e; Extended Data Fig. 3d), and this was associated with improved memory in the novel object recognition (NOR) task and the Barnes Maze hippocampal spatial memory task (Fig. f-i; Extended Data Fig. 3e–f). These findings indicate that basal TREM1 activity promotes development of age-associated inflammatory responses and cognitive decline.

To understand whether the observed cognitive rescue in aged $Trem1^{-/-}$ mice was due to altered brain microglia, we examined transcriptional changes in $CD45^{lo}CD11b^{+}$ microglia from young (3 mo) WT and aged (18–20 mo) WT and $Trem1^{-/-}$ male mice (Fig. 2a–b; Extended Data Fig. 4a–b). While there were 9.82% differentially expressed genes (1598 DEGs; FDR, $P<0.05$) in young vs aged WT microglia, there were only 0.08% DEGs (13 DEGs) in aged WT vs aged $Trem1^{-/-}$ microglia. In sharp contrast, comparison of young WT, aged WT, and aged $Trem1^{-/-}$ peritoneal MΦ revealed striking differences with 12.9% DEGs in aged WT versus young WT macrophages and 6.54% DEGs in aged $Trem1^{-/-}$ vs aged WT, but only 2.44% DEGs in the aged $Trem1^{-/-}$ vs young WT comparisons (Extended Data Fig. 4c). The relative paucity of DEGs in the aged $Trem1^{-/-}$ vs young WT comparison suggests that *Trem1* deficiency restores gene expression to youthful levels in aged MΦ. Indeed, gene expression profiles were largely reciprocally regulated in aged WT compared to both aged $Trem1^{-/-}$ and young WT MΦ (Fig. 2c; Extended Data Fig. 4d–e). Examination of the chemokine/cytokine pathway (KEGG pathway: mmu04062) revealed that young WT and aged $Trem1^{-/-}$ transcripts segregated together in reciprocal relation to aged WT macrophages (Fig. 2d). Along with the restoration of youthful pro- and anti-inflammatory surface markers in aged $Trem1^{-/-}$ peritoneal MΦ (Fig. 1d), these findings suggest that

the detrimental effects of TREM1 on cognitive aging may be mediated in large part by peripheral myeloid cells.

TREM1 deficiency restores MΦ energy metabolism in aging

Recent studies indicate that MΦ energy metabolism declines with age, leading to immune activation and pro-inflammatory polarization[29,30]. Accordingly, we performed a targeted analysis of MΦ mitochondria-related genes using Mouse MitoCarta 3.0, a curated mitochondrial gene inventory[32]. This analysis revealed a significant age-associated transcriptional increase in pathways related to ATP synthesis, electron transport, and oxidative phosphorylation in aged WT compared to young peritoneal MΦ that reverted to youthful levels in aged *Trem1*$^{-/-}$ MΦ (Fig. 2e). The paradoxical increase in mitochondrial-related transcripts in aged MΦ may reflect a compensatory response to age-associated declines in mitochondrial function. Functional assessment of MΦ bioenergetics showed significant prevention of age-associated deficits in glycolysis (extracellular acidification rate, or ECAR) and mitochondrial superoxide in aged *Trem1*$^{-/-}$ MΦ where levels were now comparable to those of young WT MΦ (Fig. 2f–g, 2j). Transmission electron microscopy (TEM) revealed that mitochondrial numbers and integrity in aged *Trem1*$^{-/-}$ MΦ were similar to those of young WT MΦ (Fig. 2h–i). The lower numbers of mitochondria in aged peritoneal MΦ may be related to the overall reduction in oxygen consumption. Taken together, transcriptomic, bioenergetic, and ultrastructural data indicate that TREM1 deficiency prevents aging of peripheral MΦ.

To further investigate how TREM1 promotes MΦ bioenergetic decline in aging, we measured 272 metabolic intermediates that are representative of a broad array of cellular metabolic pathways (Extended Data Table 1) in young (2 mo) and aged (25 mo) WT and *Trem1*$^{-/-}$ peritoneal MΦ. Principal component analysis (PCA) of young WT versus young *Trem1*$^{-/-}$ MΦ did not reveal differences between young genotypes (Extended Data Fig. 5a). A second study examining metabolic changes between young WT, aged WT, and aged *Trem1*$^{-/-}$ peritoneal MΦ showed significant differences between young and aged WT MΦ, and between aged WT and aged *Trem1*$^{-/-}$ MΦ, but not between young WT and aged *Trem1*$^{-/-}$ MΦ (Fig. 3a; Extended Data Fig. 5b–c). *Trem1* deletion restored youthful levels of multiple metabolites, and pathway analysis revealed a prominent rescue of purine, pyrimidine, and NAD^+ metabolism in aged *Trem1*$^{-/-}$ MΦ (Extended Data Fig. 5d–e). The common precursor shared by these three classes of metabolites is ribose-5P, a metabolite generated by the pentose phosphate pathway (PPP) (Fig. 3b). Aged *Trem1*$^{-/-}$ MΦ showed levels of ribose-5P that were similar to those in young MΦ.

Integration of transcriptomic data with metabolomic data confirmed a significant effect of TREM1 on purine and pyrimidine synthesis (Fig. 3c), which is dependent on sufficient supply of the precursor ribose-5P. Ribose-5P also serves as a source of glycolytic intermediates through the non-oxidative branch of the PPP, where interconversion of pentose intermediates by transketolases and transaldolases to glycolytic intermediates contributes to pyruvate generation that feeds into the Krebs cycle and fuels mitochondrial respiration. Transcripts encoding enzymes in the oxidative and non-oxidative branches of the PPP, including *G6Pdx*, *6PGd*, *RPI*, and *Taldo1* were reduced in aged WT but restored to youthful

levels in aged *Trem1*$^{-/-}$ macrophages (Fig. 3d). Transcription factor enrichment analysis revealed that the top transcription factor associated with these metabolic changes was NRF2 (Extended Data Fig. 5f), which reprograms metabolic transcription to promote nucleotide metabolism[33] and declines with aging[34]. Indeed, confocal microscopy quantification of MΦ NRF2 in young vs aged peritoneal MΦ demonstrated lower levels of NRF2 in aged MΦ that were restored to youthful levels in aged *Trem1*$^{-/-}$ mice (Fig. 3e–f; Extended Data Fig. 5g). Taken together, metabolomic and transcriptomic data support a role for TREM1 in regulating generation of the critical intermediate ribose-5P through activity of the oxidative and non-oxidative branches of the PPP. Declines in NRF2-dependent PPP gene expression with aging lead to deficits in ribose-5P, which is not only the precursor of purines and pyrimidines, but also fuels the non-oxidative PPP that supports glycolysis and pyruvate production. By restoring the PPP, *Trem1* deficiency raises levels of acetyl-coA, which in addition to being generated from fatty acid metabolism, is also generated by pyruvate dehydrogenase from pyruvate (Extended Data Fig. 5h) and is the entry point of carbohydrates into the TCA that fuels mitochondrial respiration.

TREM1 deficiency in 5XFAD mice prevents memory deficits

While aging is the primary risk factor for AD, deposition of amyloid is necessary, but not sufficient for progression to AD[35]. We therefore tested whether microglial TREM1 might regulate cellular responses to oligomeric amyloid ß$_{42}$ (Aß$_{42}$), a highly immunogenic form of amyloid that accumulates in AD (Fig. 4a–b). Indeed, TREM1 activation in WT microglia in response to Aß$_{42}$ oligomers suppressed mitochondrial oxidative phosphorylation and increased glycolysis, however *Trem1*$^{-/-}$ microglia were completely refractory to the effects of Aß$_{42}$ and maintained homeostatic bioenergetics, reminiscent of the protective effect of *Trem1* deficiency in aging macrophages. We therefore hypothesized that microglial TREM1 may play a role in mediating the neurotoxic effects of locally accumulating amyloid.

Flow cytometry of microglia in the 5XFAD model[36] of amyloid accumulation showed low TREM1 surface expression that did not differ from age-matched WT controls (Fig. 4c). Similarly, in the *APP*^{Swe}*PS1*$^{\Delta E9}$ model[37] of amyloid accumulation, immunostaining of TREM1+ Iba1+ microglia did not show a significant induction of TREM1 expression compared to WT (Extended Data Fig. 6a), suggesting that microglial TREM1 expression is not significantly changed in the context of accumulating amyloid. To determine whether TREM1 might nevertheless promote cognitive deficits in the context of amyloid and independently of age, we examined 6–7 mo 5XFAD mice that were heterozygous for *Trem1*. *Trem1* haploinsufficiency in 5XFAD mice prevented cognitive deficits in both the novel object recognition (NOR) memory test and Barnes maze test of spatial learning and memory (Fig. 4d–e). There were no differences in levels of dense core or diffuse amyloid plaque or in levels of soluble and insoluble Aß$_{42}$ (Fig. 4f–g; Extended Data Fig. 6b–d). Several immune factors were altered between 5XFAD and 5XFAD;*Trem1*$^{+/-}$ hippocampi (Fig. 4h; Extended Data Fig. 6e). Examination of microglial morphology revealed a striking preservation of resting characteristics in 5XFAD;*Trem1*$^{+/-}$ mice, where microglia remained homeostatic and not activated, with average and maximal branch lengths indicative of a surveilling phenotype (Fig. 4i–j; Extended Data Fig. 6f).

To investigate the molecular mechanisms underlying this preservation of homeostatic morphology, we examined transcriptional differences in $CD45^{lo}CD11b^{+}$ microglia isolated from 6–7 mo male WT, 5XFAD and 5XFAD; $Trem1^{+/-}$ mice. We observed the expected transition from WT to the disease-associated microglial signature[15] (DAM) in 5XFAD microglia, but there were no significant differences between 5XFAD and 5XFAD; $Trem1^{+/-}$ DAM signatures (Extended Data Fig. 7a–c). Although not significant, there was a trend in 5XFAD; *Trem1+/−* microglia towards higher homeostatic transcript levels and selected Stage 1 and Stage 2 phagocytic/inflammatory DAM genes[15] (Fig. 4k). Consistent with the muted effect on the DAM signature, we did not observe significant changes by flow cytometry in homeostatic markers CX3CR1 and Tmem119 between 5XFAD and 5XFAD; *Trem1+/−* microglia (Extended Data Fig. 7d–e). However, quantification of BACE1 immunostaining at amyloid plaques, a marker of neuritic dystrophy[38], was significantly reduced in 5XFAD; $Trem1^{+/-}$ as compared to 5XFAD mice, suggesting a neuroprotective effect of *Trem1* haploinsufficiency (Fig. 4l–m). We also identified a restoration to WT levels of several plasma cytokines in 9–10 mo 5XFAD; $Trem1^{+/-}$ mice (Fig. 4n), suggesting a potential peripheral effect of *Trem1* haploinsufficiency. Taken together, these data suggest a protective role of TREM1 deficiency that is independent of amyloid and microglial transcriptional responses to amyloid.

Beneficial effects of TREM1 deficiency in aged APP^{Swe} mice

We also investigated the functional consequences of TREM1 activity in a second model, the TG2576 APP^{Swe} model of amyloid accumulation[39]. APP^{Swe} mice develop progressive hippocampal memory deficits beginning at 6 months of age and amyloid plaques after 12 months of age. We examined the role of TREM1 in the interaction of aging and amyloid deposition, the context in which AD develops. In the novel objection recognition test, memory was disrupted in aged 18–21 mo male and female APP^{Swe} mice compared to WT littermates, however loss of one or both *Trem1* alleles restored memory to WT levels (Fig. 5a). In the Barnes maze, spatial memory was significantly rescued in APP^{Swe};$Trem1^{-/-}$ mice as compared to WT littermates (Fig. 5b; Extended Data Fig. 7g–h). As in the 5XFAD model, this behavioral rescue occurred in the absence of changes in amyloid deposition (Fig. 5c–d). Selected hippocampal immune factors were increased in APP^{Swe} with variable effects of *Trem1* deficiency; however in plasma, increases in inflammasome products IL1α and IL1ß were elevated in APP^{Swe} mice but restored to WT levels with *Trem1* deficiency (Fig. 5e–f). These data indicate that TREM1 promotes a systemic pro-inflammatory state in the context of aging and accumulating amyloid.

Healthy neuronal mitochondrial function is critical for neurotransmission and circuit integrity, so we investigated whether myeloid TREM1 regulates bioenergetic function of synaptic mitochondria isolated from synaptosome fractions of APP^{Swe} mice lacking one or both *Trem1* alleles. We determined the extent of coupling between the electron transport chain (ETC) and oxidative phosphorylation of ADP to ATP in synaptosomes[29,40]. The respiratory control ratio (RCR), represented as the ratio of State III/State IVo, was significantly reduced in 18–24 mo APP^{Swe} mice as compared to age-matched WT mice, consistent with poor neuronal mitochondrial function (Fig. 5g–h). However, loss of one or both *Trem1* alleles restored synaptic mitochondrial function to WT levels. The improved

coupling of electron transport and ATP synthesis suggests that in the setting of accumulating amyloid, *Trem1*-deficient microglia maintain homeostatic immune responses that preserve healthy synaptic mitochondrial function.

Using an orthogonal approach to measure neuronal metabolic function, we assessed cerebral glucose metabolism using positron emission tomography (PET) and the glucose analogue tracer 2-deoxy-2-^{18}F fluoro-D-glucose ([^{18}F]FDG PET) in 17–19 mo female APP^{Swe} mice. Although [^{18}F]FDG PET reliably demonstrates hypometabolism in human parietal cortex in patients with AD, in transgenic mutant APP models, [^{18}F]FDG PET signal can vary depending on experimental factors such as anesthesia, type of APP mutation, and age[41]. Here, compared to wild type controls, APP^{Swe} hippocampus and thalamus showed a significant increase in glucose uptake that was prevented with deletion of one or both *Trem1* alleles (Fig. 5i–j). The normalization of brain glucose metabolism with partial or complete *Trem1* deficiency suggests that accumulating amyloid in APP^{Swe} mice triggers TREM1-dependent microglial responses that disrupt brain glucose metabolism. Together, these results suggest that *Trem1* deficiency preserves cellular and cerebral bioenergetics in aging APP^{Swe} mice.

TREM1 expression increases in Alzheimer's Disease

To determine the cellular localization of TREM1 in AD, we carried out immunofluorescent colocalization studies of TREM1 in Iba1+ cells in free-floating sections from control and AD post-mortem frontal cortex. TREM1 expression in AD brain colocalized to Iba1+ cells that were morphologically round and clustered around X34+ amyloid plaques (Fig. 6a; Extended Data Fig. 8a). However, TREM1 was not present in all Iba1+ cells and was not expressed in classically ramified Iba1+ microglia. Moreover, numbers of TREM1+Iba1+ cells were highest around amyloid plaques, with fewer present in amyloid-free areas in AD brain, and even fewer in control brain (Fig. 6b).

We also investigated the relationship between TREM1 expression and increasing levels of Braak pathology, the basis for neuropathological diagnosis of AD[42]. TREM1 levels were assayed in middle frontal gyrus, or BA 9/46[43], a brain region that in AD demonstrates a severe bilateral gray matter loss[44], synaptic loss, and high Aβ burden[45]. The tissue was obtained from subjects classified as: non-demented (Braak I–II, n = 12), non-AD demented Braak I–II (n = 12), AD Braak III–IV (n = 12) and AD Braak V–VI (AD-high, n = 12). Diagnostic groups were balanced for age, gender, and post-mortem interval. Demographic information of the cohort is shown in Extended Data Table 2. Quantification of protein levels by immunoblotting revealed a steady increase of both TREM1 and TREM2 in frontal cortical lysates from non-demented, non-AD demented Braak I-II, AD-Braak III-IV, and AD-Braak V-VI donors (Fig. 6c–d and Extended Data Fig. 8b–c). The fold change increase over control was identical for TREM1 and TREM2 at 1.24-fold. Thus, both TREM1 and TREM2 increase with clinical AD progression, reaching significance at the AD-Braak V-VI stage which is characterized by extensive neocortical involvement of neurofibrillary tangles (NFTs) along with high Aß plaque burden in the frontal cortex. This parallel increase may be reflective of increasing microglia/macrophage numbers with progression of AD[46]. TREM1 levels were positively associated with both amyloid and tau pathology,

whereas TREM2 levels were positively associated with tau pathology alone (Fig. 6e–f). The relationship between TREM2 and tau is supported by cerebrospinal fluid (CSF) soluble TREM2 (sTREM2) biomarker data, where increased levels of CSF sTREM2 are observed in patients and controls with increased tau pathology[47,48].

Recent advances in GWAS methods have allowed a deeper look into variants that confer increased AD risk. An example is Mendelian randomization (MR). In a two-step process, MR first trims the list of potential gene variants by retaining only those that have a significant effect on the corresponding protein level. In the second step, GWAS is performed on this smaller list of variants, thereby increasing statistical power to detect associations between variants and outcomes that may exist. A recent study applying MR to plasma proteins found that an increase in plasma levels of the soluble ectodomain of TREM1, or sTREM1, was associated with increased AD risk[49]. We validated this finding independently using plasma proteins measured using a multiplexed, aptamer-based approach (SOMAscan assay) in 35,559 Icelanders[50] to determine which variants associated with plasma sTREM1 and sTREM2. We then assessed AD risk associated with these variants in a second cohort of 75,024 cases and 397,844 controls from the UK Biobank[51]. These MR associative analyses indicated that both sTREM1 and sTREM2 levels were causally associated with AD risk (Fig. 6g–h and Extended Data Fig. 8d). Increased sTREM1 levels were associated with increased AD risk and conversely, increased sTREM2 levels were associated with decreased AD risk. Together, the above findings indicate that TREM1 expression increases with increasing amyloid and tau burden and positively associates with AD risk.

DISCUSSION

Although significant interest has centered on the protective microglial phenotype promoted by TREM2 in amyloid accumulation in AD, our findings point to its functional counterpart, TREM1, as a potent driver of age- and amyloid-dependent myeloid dysfunction and cognitive decline. In the setting of physiological aging, transcriptomics indicate that peripheral myeloid TREM1 in large part drives age-associated inflammation and cognitive decline. Metabolomic analysis revealed that with aging, basal TREM1 expression suppressed glucose metabolism, particularly the generation of ribose-5P that is critically required for both glycolysis and biosynthesis of purines, pyrimidines, and NAD+. In contrast, preclinical modeling in transgenic models of amyloid accumulation, a necessary event for development of AD[35], revealed a TREM1-dependent disruption of spatial memory that was associated with both peripheral and microglial immune changes. The phenotypic rescue from TREM1 deficiency was independent of amyloid accumulation. In 5XFAD mice, *Trem1* haploinsufficiency preserved homeostatic microglial morphology and reduced neuritic dystrophy, a rescue that occurred in the absence of changes in the DAM signature, a transcriptional pattern that reflects microglial responses to accumulating amyloid. In aging APP^{Swe} mice, loss of one or both *Trem1* alleles also prevented cognitive decline independently of amyloid and elicited a neuroprotective effect by normalizing synaptic mitochondrial integrity and cerebral glucose uptake. In human postmortem brain, increasing TREM1 expression in Iba1+ myeloid cells positively associated with increasing amyloid and tau pathologies in AD subjects. Thus, TREM1 functions as a negative regulator of myeloid

bioenergetics and homeostatic immune responses and promotes cognitive decline in both aging and amyloid accumulation.

Flow cytometry measurements demonstrated relatively low levels of surface TREM1 expression in microglia as compared to peripheral myeloid cells in young and aged mice. This would suggest a minimal contribution of microglial TREM1 to disrupted neuronal function in aging. This conclusion was supported by transcriptomic analyses, which showed significant changes between *Trem1*-deficient and WT genotypes in aged peripheral macrophages but negligible changes in aged microglia, and metabolomic analyses of peripheral MΦ, where youthful bioenergetics were maintained in aged *Trem1*-deficient mice. The mechanisms by which *Trem1*-deficient peripheral myeloid cells regulate neuronal function may include beneficial conditioning of the blood and blood-brain barrier from improved MΦ function throughout the periphery.

In 5XFAD mice, there was no significant induction of TREM1 surface expression on microglia, a finding in line with the muted microglial transcriptional response to *Trem1* haploinsufficiency. However, microglia in 5XFAD;$Trem1^{+/-}$ mice demonstrated resilience and maintained their homeostatic morphology consisting of a non-activated, surveilling phenotype. A potential explanation may reside in the finding that *Trem1*-deficient microglia are refractory bioenergetically to the immunogenic effects of amyloid-ß and therefore do not launch immune responses to local stimuli like amyloid peptides that are neurotoxic. It is possible that microglial TREM1, even at low expression levels, mediates neurotoxic effects, a possibility that is supported by the significant decrease in neuritic dystrophy in 5XFAD;$Trem1^{+/-}$ mice. However, given the restoration to WT levels of plasma cytokines in 5XFAD;$Trem1^{+/-}$ mice, it is possible that there is also a peripheral neuroprotective effect of *Trem1* haploinsufficiency in addition to a protective microglial effect (Extended Data Fig. 7j).

In the APP^{swe} model of amyloidosis, immune activation is linked to increased brain glucose uptake visualized by PET. While it remains unclear what cell type is driving the PET signal in AD mice, our FDG-PET findings are in line with a recent study suggesting that microglia may contribute directly, or indirectly via activation of astrocytes, to FDG uptake in models of amyloidosis[52,53]. Loss of one or both *Trem1* alleles restores glucose uptake in APP^{Swe} mice to WT levels, suggesting that myeloid TREM1, peripheral and/or microglial, promotes glial activation and demand for glucose. Our analyses of synaptic mitochondrial bioenergetics in APP^{swe} mice showed prominent deficits – prevented in both $Trem1^{+/-}$ *and* $Trem1^{-/-}$ genetic backgrounds – that might potentially lead to compensatory increases in glucose uptake in APP^{swe} mice. However other cell types, particularly astrocytes, may also be driving glucose uptake. Thus, the normalization of the FDG-PET signal with loss of one or both *Trem1* alleles may reflect changes in additional cell types directly and indirectly affected by TREM1-mediated changes in microglia. Our bioenergetic assay on neuronal mitochondria used succinate, a substrate of Complex II which allowed us to specifically measure Complex II mediated respiration, which was rescued with loss of one or both *Trem1* alleles. Not performed in this study was the interrogation of Complex I-mediated electron transport using the substrate pyruvate which would provide an additional measure of mitochondrial respiration. Overall, our findings support the emerging concept that cellular

metabolism – in microglia and peripheral macrophages – is a major regulator of immune responses that regulate cognitive function in aging and neurodegeneration.

Mendelian Randomization confirmed *TREM1* as a genetic risk factor for AD and demonstrated that genetic variants associated with higher plasma sTREM1 are also associated with increased AD risk. In a large cohort of well-characterized donor samples, quantitative immunoblotting revealed a significant increase in TREM1 with increasing Braak staging that predicted amyloid neuritic plaque and tau neurofibrillary tangle burden. Immunofluorescent staining revealed prominent TREM1+/Iba1+ cells in proximity (within 15 um) of amyloid plaques as well as an increase in TREM1+/Iba1+ cells in non-plaque associated regions in AD compared to control brain. These cells appeared rounded and many were located near blood vessels. Together, these findings raise the possibility that plaque-associated TREM1+ cells may represent infiltrating macrophages, highlighting the link between peripheral immune cells and amyloid and tau neuropathology in AD.

Systemic and brain inflammation are major contributing factors to the initiation and progression of age-associated cognitive decline and neurodegeneration. Our findings demonstrate a highly detrimental role of basal TREM1 signaling in aging driven by its disruption of myeloid glucose and nucleotide metabolism. In the aging brain, and in the aging brain that is accumulating amyloid, TREM1-mediated disruption of homeostatic and youthful bioenergetics promotes immune responses that are neurotoxic. These findings suggest an alternative approach to diseases of aging, where myeloid cells might be reprogrammed to a healthier metabolic phenotype, providing a critical disease-modifying effect needed to slow or halt progression to AD.

METHODS

Animals

This study was conducted in accordance with National Institutes of Health (NIH) guidelines and the Institutional Animal Care and Use Committee at Stanford University approved protocols. *Trem1*$^{-/-}$ mice on a C57BL/6 genetic background have been previously described[54] and were crossed with either 5XFAD[55] (B6SJL-Tg(APPSwFlLon,PSEN1*M146L*L286V)6799Vas/Mmjax, JAX MMRRC Stock# 034840, Jackson Labs) or *APP*^{Swe} mice [39] (B6;SJL-Tg(APPSWE)2576Kha, Taconic stock # 1349) or with C57BL/6J mice (Jackson Labs). All mice were socially housed in an environment controlled for lighting (12 hour light/dark cycle), temperature (18–23°C), and humidity (40–60%), with food and water available *ad libitum.* The Stanford Veterinary Service Center monitors and maintains pathogen-free mouse housing as described in http://med.stanford.edu/vsc/about/rodent-handbook/rodent-diseases.html.

Flow cytometry of microglia, peripheral myeloid cells, and peritoneal macrophages

Mice were terminally anaesthetized. Blood and splenocytes were collected and lysed with ACK lysis buffer for 10 min at room temperature. All cells were then resuspended in FACS buffer. Dead cells were excluded by staining with Live/dead Aqua (Thermo Fisher). Cells were stained with antibodies for 30 min on ice. Microglial purity was confirmed by CD11B-

A700 (Thermo Fisher, clone M1/70), CD45-BUV395 (BD Biosciences, clone 104), Gr1-V450 (Thermo Fisher, clone RB6–8C5), and CD206-BV605 (Biolegend, clone C068C2). Microglial homeostasis was examined by CX3CR1-PE/Cy7 (Biolegend, clone SA011F11), P2RY12-PE (Biolegend, clone S16007D), and Tmem119-FITC (Thermo Fisher, clone V3RT1GOsz). TREM1 expression in microglial was examined by Trem1-APC (R&D, clone 174031). Cells were centrifuged, washed, and resuspended in FACS buffer for flow cytometry on an LSR II (BD Biosciences) with FACSDiva software (v9.0, BD Biosciences). FlowJo software (v10, FlowJO, Ashland, OR) was used for the analysis and depiction of the gating strategy.

Peritoneal macrophages were collected from terminally anaesthetized WT and *Trem1*$^{-/-}$ mice. The peritoneal space was flushed with 10 mL ice-cold PBS. Collected cells were added to 1 mL of ACK lysis buffer (Cat# A1049201, Thermo Fisher Scientific) for 5 minutes at room temperature. The prepared samples were then washed with FACS buffer (500 mL PBS, 1g BSA, 1mL 5M EDTA) and centrifuged at 500 g for 3 minutes. Cells were resuspended in FACS buffer containing 1:200 of primary antibodies: CD11b-BV421 (Cat# 101235, Biolegend), Ly6G-BV605 (Cat# 563005, Biolegend), LY6C-V450 (Cat# 560594, Biolegend), CD86-APC (Cat# 105012, Biolegend), CD45-AF700 (Cat# 560510, Biolegend), MHCII-FITC (Cat# 11–5321-82, Thermo Fisher Scientific), CD71-PerCP/Cyanine5.5 (Cat# 113816, Biolegend), Live/Dead-Aqua (Cat# L34957, Thermo Fisher Scientific), and incubated for 20 minutes at 4°C. Cells were centrifuged at 500 g for 3 minutes, washed one time with FACS buffer, and resuspended in 4% PFA for 25 minutes at 4°C. After fixation, cells were washed twice and resuspended in FACS buffer until flow cytometric analysis.

Microglia for RNA-seq: Mice were terminally anaesthetized and perfused with ice-cold HBSS. Brain hemispheres were cut into small pieces with a razor blade and homogenized by Dounce in a solution of HBSS containing 15 mM HEPES, 0.5% glucose, 12.5 KU/ml DNase I, and 0.1 U/ml RNAase inhibitor. Brain homogenates were filtered through a 70-μm strainer followed by myelin removal using myelin removal beads (Miltenyi Biotec). Cells were resuspended in FACS buffer (2% FBS in PBS) and stained for 30 min with anti-CD45-PE (Thermo Fisher, clone 104) and anti-CD11b-Alexa Fluor 700 (Thermo Fisher, clone M1/70). Dead cells were excluded by staining with Live/dead Aqua (Thermo Fisher). Cell sorting was performed on an ARIA II (BD Biosciences) with FACSDiva software (v9.0, BD Biosciences). $CD45^{low}CD11b^{+}$ cells were defined as the microglial population and were sorted directly into buffer RLT (Qiagen) and stored at −80 °C. The resulting microglia from two pooled mouse brains/sample yielded on average 80,000 $CD45^{low}CD11b^{+}$ cells and were processed for bulk RNA-seq experiments. FlowJo software was used for analysis and depiction of the gating strategy.

Chemokine and cytokine multiplex assay

Chemokine and cytokine analysis was carried out at the Human Immune Monitoring Core (Stanford University) or Eve Technologies (Calgary, Alberta, Canada) using magnetic bead-based multiplex Luminex assays (Cat# LXSAMSM, R&D Systems, Inc., Minneapolis, MN).

Plates were read using a Luminex LabMap200 instrument. Mean fluorescence intensity (MFI) was averaged over duplicate wells for each cytokine per sample on each plate.

Novel object recognition (NOR) task

Novel object recognition was performed as previously described[56]. Briefly, mice were habituated to an empty arena (40 cm × 40 cm × 35 cm) containing wall-mounted visual cues for 5 minutes. Mice were then given one 5 min trial during which they explored two identical objects in fixed positions in the middle of the arena. Animals were randomly assigned to identical starting objects of either 25 mL cell culture flasks filled with sand or LEGO towers (3 cm × 3 cm × 7.5 cm). In the testing phase, mice explored the same arena for 5 min but with one object replaced by a novel, distinct object. Interactions with objects (sniffing or exploring within 2 cm of object; excluding time spent sitting on top of object) were manually timed in a blinded fashion to assess the fraction of time spent exploring each object (single object interaction time/total interaction time with both objects). Between trials, the arena and objects were thoroughly cleaned with 10% EtOH.

Barnes maze task

The Barnes maze test was performed as previously described with adaptations to accommodate aged and AD model mice[56]. Briefly, a large circular maze containing 16 holes on the outer edge was centered over a pedestal and elevated approximately 3 feet above the floor. All holes were open to the floor except for the escape hole. The escape hole consisted of a PVC elbow joint connector. Distinct visual cues were placed at four equally spaced points around the maze. An overhead light, two additional standing lights, and a fan blowing on the maze provided motivation to find the escape hole while also serving as supplemental visual cues. The escape hole position was fixed for all trials. Mice performed four trials per day for four consecutive days, as follows. For the adult WT, aged WT, and aged *Trem1−/−* cohorts, the starting location of the mouse was moved relative to the escape hole position every trial. For the 5XFAD and aged APP^{Swe} cohorts, the starting location remained unchanged for all trials. Escape Latency is defined as the time for a mouse to enter the escape hole. If any mouse failed to locate the escape hole within 90 seconds, they were gently guided by light tapping towards the escape hole and assigned an escape latency score of 90 seconds. The maze and escape holes were thoroughly cleaned with 10% EtOH after every trial. Testing was performed by an investigator blinded to experimental conditions.

Peritoneal Macrophages

Peritoneal macrophages were collected from terminally anaesthetized *Trem1−/−* and WT male mice. Mice were injected intraperitoneally with 1.5 ml 3% (w/v) thioglycolate medium (Cat# 211716, BD Biosciences) for Seahorse experiments, and peritoneal macrophages were isolated 3–4 days later by flushing with ice-cold 1× PBS buffer (Corning). For metabolomics and RNA-seq experiments, peritoneal macrophages were collected by lavage and enriched using CD11b MicroBeads (Cat# 130–049-601, Miltenyi Biotec, San Jose, CA) following the directions provided by the manufacturer. Cells were seeded at a density of 3×10^6 cells per well in DMEM supplemented with 10% heat-inactivated fetal bovine serum (FBS; Cat# F4235, Sigma-Aldrich), 100 U ml^{-1} penicillin and streptomycin, and maintained at 5%

CO_2 at 37 °C. After overnight culture, cells were washed twice with medium to remove nonadherent cells.

RNA Sequencing and analysis

Bulk RNA extraction and sequencing were performed by Novogene, Inc (Sacramento, CA). RNA degradation and contamination was monitored on 1% agarose gels and RNA purity was verified using the NanoPhotometer® spectrophotometer (IMPLEN, CA, USA). RNA integrity and quantification were assessed using the RNA Nano 6000 Assay Kit of the Bioanalyzer 2100 system (Agilent Technologies, CA, USA). Total mRNA was transcribed into full length cDNA using Takara V3 Stranded Prep kit (Cat. 634485, Takara Bio USA, Inc., Mountain View, CA). Clustering of index-coded samples was performed on a cBot Cluster Generation System using PE Cluster Kit cBot-HS (Illumina) according to the manufacturer's instructions. After cluster generation, the library preparations were sequenced on an Illumina platform and paired-end reads were generated. Raw data (raw reads) in FASTQ format were processed through fastp. In this step, clean data (clean reads) were obtained by removing reads containing adapter and poly-N sequences and reads with low quality. At the same time, Q20, Q30 and GC content of the clean data were calculated. All downstream analyses were based on clean data of high quality. Reference genome and gene model annotation files were downloaded from the genome website browser (NCBI/UCSC/Ensembl) directly. Paired-end clean reads were aligned to the reference genome using the Spliced Transcripts Alignment to a Reference (STAR) software (v2.6.1d). FeatureCounts (v1.5.0-p3) was used to count read numbers mapped for each gene. Differential expression analysis between two conditions/groups was performed using DESeq2 (v1.20.0) using default settings. DESeq2 provides statistical routines for determining differential expression in digital gene expression data using a model based on the negative binomial distribution. The resulting P values were adjusted using the Benjamini and Hochberg's approach for controlling the False Discovery Rate (FDR). Genes with an FDR-adjusted P value (q-value) < 0.05 by DESeq2 were designated differentially expressed. Enrichment analysis of DEGs was performed using the Gene Ontology (GO) enrichment analysis tools with the PANTHER classification system (v18). Hypergeometric testing was performed to assess overrepresentation of DEGs ($q < 0.05$) within relevant gene sets including lysosome, phagocytosis, cytokines and chemokines.

Seahorse Assay for Real-Time Oxygen Consumption Rate (OCR) and Extracellular Acidification Rate (ECAR) Mouse peritoneal macrophages or primary microglia were plated at 1.8×10^5 cells per well in a Seahorse XF24 Cell Culture Microplate (Agilent, Santa Clara, CA, USA). Cells were washed twice with Agilent Seahorse XF Media (Agilent) supplemented with 1 mM sodium pyruvate, 2 mM L-glutamine, and 10 mM D-glucose; a final volume of 500 µl was placed in each well. Cells were incubated in a 0% CO_2 chamber at 37°C for 1 hr before being placed into a Seahorse XFe24 Analyzer (Agilent). Cells were treated with 1 µM Oligomycin, 1 µM FCCP, and 0.5 µM rotenone/antimycin. A total of three OCR and pH measurements were taken per condition. For peritoneal macrophages, the experiment was repeated 6 times. For the first 3 experiments, the Seahorse assay was normalized by the number of cells in each well measured after the completion of the assay. OCR values were adjusted by multiplying by sample/well specific normalization factor

using the Wave software. As no significant difference between starting number of cells and number of cells at the end of the assay was observed following normalization, the subsequent 3 assays were performed without post-assay normalization adjustment.

Transmission Electron Microscopy (TEM)

Primary peritoneal mouse macrophages (2×10^6 cells/ml) were isolated. Briefly, cells were fixed in 2% glutaraldehyde and 4% paraformaldehyde in 0.1 M sodium cacodylate (pH 7.4), treated with 10% gelatin solution in sodium cacodylate buffer, and incubated with 2% osmium tetroxide. Cell pellets were stained with 1% uranyl acetate, dehydrated in ethanol, and embedded in resin (EPON epoxy resin). Sections were generated using a Leica EM UC7 ultramicrotome (Leica Microsystems) at 50 nm and placed within grids stained with a 1:1 mix of 3% uranyl acetate, 50% acetone for 30–60 s. Grids were imaged with a JEM 1400 transmission electron microscope (JEOL) at ×1,200 for low magnification and ×12,000 for high magnification (unless otherwise noted) using Gatan Microscopy Suite software (v3, Gatan, Inc., Pleasanton, CA). Images were quantified by an individual blinded to experimental conditions in ImageJ. Abnormal mitochondria were defined as containing at least one of the following features: paracrystalline inclusions, linearization of cristae and abnormal angular features, concentric layering of cristae membranes, matrix compartmentalization, nanotunneling, in combination with doughnut-shaped or balloon-shaped mitochondria. Mitochondria measurements were completed using NIH ImageJ software (National Institutes of Health, USA) by investigators blind to experimental conditions.

Mitochondrial Superoxide Assay

Peritoneal macrophages were plated at a density of 25×10^4 cells in DMEM, 10% FBS and 1% PS per well in a 96-well plate and cultured overnight at 37°C and 5% CO_2. Media was replaced the following day. Mitochondrial Superoxide Assay Kit (Abcam, Cat# ab219943) and MitoTracker Deep Red FM (Invitrogen, M22426) were used to measure mitochondrial superoxide production and content exactly as described in manufacturer's directions. Plates were read on fluorescence plate reader.

Targeted metabolomics

Metabolites were extracted from CD11b-purified primary peritoneal macrophages in a 80:20 methanol:water solution in a volume of 75 mL solvent per 1-million cells, vortexed, incubated on dry ice for 10 min, and centrifuged at 16,000 g for 20 min, and the supernatant was assayed by LC-MS analysis. Extracts were analyzed within 24 hr by liquid chromatography coupled to a mass spectrometer (LC-MS). The LC–MS method involved hydrophilic interaction chromatography (HILIC) coupled to the Q Exactive PLUS mass spectrometer (Thermo Scientific)[57]. The LC separation was performed on an XBridge BEH Amide column (150 mm 3 2.1 mm, 2.5 mm particle size, Waters, Milford, MA). Solvent A was 95%: 5% H2O: acetonitrile with 20 mM ammonium bicarbonate, and solvent B was acetonitrile. The gradient was 0 min, 85% B; 2 min, 85% B; 3 min, 80% B; 5 min, 80% B; 6 min, 75% B; 7 min, 75% B; 8 min, 70% B; 9 min, 70% B; 10 min, 50% B; 12 min, 50% B; 13 min, 25% B; 16 min, 25% B; 18 min, 0% B; 23 min, 0% B; 24 min, 85% B; 30 min, 85% B. Other LC parameters are: flow rate 150 ml/min, column temperature 25°C,

injection volume 10 mL and autosampler temperature was 5°C. The mass spectrometer was operated in both negative and positive ion mode for the detection of metabolites. Other MS parameters were: resolution of 140,000 at m/z 200, automatic gain control (AGC) target at 3e6, maximum injection time of 30 ms and scan range of m/z 75–1000. Raw LC/MS data were converted to mzXML format using the command line "msconvert" utility[58]. Data were obtained with MAVEN software[59,60].

Metabolomics data analysis was carried out using MetaboAnalyst version 5.0[61]. Metabolomic data were log-transformed and scaled according to the auto-scaling feature (mean-centered and divided by the standard deviation of each variable). Metabolites that were significantly different by ANOVA (with FDR correction) were subjected to hierarchical clustering analysis using the Euclidian distance measure and Ward clustering algorithm. Differentially expressed metabolites by volcano plot underwent pathway-based enrichment analysis using 84 metabolite sets based on KEGG human metabolic pathways in MetaboAnalyst 5.0.

Integration of transcriptomic and metabolomic features

Integration of macrophage RNA-seq and metabolomic data was performed using the Joint Pathway Analysis feature in MetaboAnalyst 5.0. Enrichment analysis was carried out by hypergeometric test with degree centrality selected as topology measure. A loose integration method was applied such that enrichment analysis was performed separately for genes and metabolites in their "individual universe" then the individual *P*-values were combined via weighted *Z*-tests. Weights were based on the overall proportion of each omics within the "universe". Significantly enriched pathways were determined by applying the cutoff of $q < 0.05$.

Immunocytochemistry of NRF2 in peripheral macrophages

Primary macrophages were collected by peritoneal lavage of ice-cold PBS. Cells were maintained in DMEM/F12 + 10% FBS + 1% PS solution at 5% CO_2 at 37°C. After overnight culture, cells were washed twice with media to remove nonadherent cells and were further cultured for an additional 24-hours. Cells were washed twice with PBS to remove media and cells were fixed with ice-cold 100% methanol for 12 minutes at −20°C. Methanol application results in denaturation and dehydration of proteins, allowing for unmasking of epitopes. Cells were then washed 3 × with PBS with 0.1% Tween 20, and then blocked for 1 hour with 1% BSA and 10% NGS with 0.1% Tween 20. Coverslips were incubated with antibodies to NRF2 (1:500, Cat# ab62352, Abcam) and CD11b (1:2000, Cat# NB600–1327, Novus Biologicals, Centennial CO). Coverslips were washed, stained with DAPI, and coverslipped as before. Z-stack images of CD11b+ cells spanning 15 μm were captured using Zeiss LSM 980 inverted confocal microscope using the 63x oil objective. A loss of nuclear localization of DAPI-stained DNA has been described with methanol fixation. NRF2 signal was measured within each z-plane using ImageJ.

Primary Microglial Cultures

Postnatal day 1–3 C57/BL6 mice were euthanized and hippocampus and cortex were harvested, removing meninges under a dissection microscope. Brains were trypsinized for

25 min, with agitation every 5 min. Trypsinization was stopped with Trypsin inhibitor (0.6 mg/ml) in DMEM/F12 + 10% FBS + 1% PS solution. Tissue was homogenized and then passed through a 100 μm cell strainer. Cells were plated in a T-175 cm^2 flask and incubated in 5% CO_2, 37°C incubator for 5 days in DMEM/F12 + 10% FBS + 1% PS. After 5 days, media was changed and cells were allowed to sit for another 9 days (14 days total, changing media every 5 days). Mixed cultures were then shaken for 8 h at 225 rpm and microglial cells were resuspended in DMEM+10% FBS + 1% PS and plated at a confluency of 1.8 × 10^5 per well in an XF24 Seahorse plate. Cells were treated with amyloid-beta oligomers ($Aß_{42}$ oligomers; 100 nM) or veh for 20 hr and Seahorse was carried out as described below.

Immunofluorescent staining of mouse brain

Coronal tissue sections containing the dorsal CA1 region of the hippocampus were washed with PBS containing 0.3% Triton X-100. Sections were blocked in 10% NDS for 1 hour then incubated overnight in primary antibody solution containing anti-Iba1 (1:1000, Cat# 019–19741, Wako) and 6E10 (1:1000, Cat# 803001, BioLegend, San Diego, CA) in 5% NGS. Sections were washed 3 × 10 min and incubated for 2 hours at RT with secondary antibodies (Abcam). Sections were again washed and stained with DAPI for 10 min. After a final wash in PBS, sections were mounted on glass slides and coverslipped using ProLong Gold Antifade reagent (ThermoFisher). For quantification of mature amyloid plaques, sections were incubated with Thioflavin S. Tissue was imaged using a Zeiss LSM 980 inverted confocal microscope running version 3.3 Zen Blue software (Zeiss, Dublin, CA). Images containing the CA1 region of the hippocampus were captured in z-plane spanning 15 μm with a step-size of 0.5 μm. An ImageJ macro was used to automatically z-project image stacks, despeckle, enhance contrast and skeletonize the IBA1 signal. The software plugin AnalyzeSkeleton (2D/3D) was used to calculate average and maximal branch length as previously described[62]. Representative images were prepared using ImageJ and Imaris software (Version 9.9.1, Oxford Instruments, Abingdon, UK).

For analysis of neuritic dystrophy, tissue sections spanning the dorsal hippocampus were washed 3x in PBS-T and then incubated for 20 minutes in 10 μMol X34 (SML1954, Milipore Sigma) solution prepared in 40% EtOH in PBS in 0.02N NaOH at room temperature. After incubation with X34, sections were washed in 40% EtOH and then PBS. Sections were then blocked for 1 hour in 10% NGS and incubated overnight in rabbit anti-BACE1 antibody (1:500, Cat#108394, Abcam). The following day tissue sections were washed and incubated with secondary antibody (Abcam). Sections were washed then mounted on glass slides and coverslipped with ProLong Gold antifade reagent (ThermoFisher). Slides were imaged using a LSM 980 Confocal microscope at 63X magnification. Three images were acquired each from 3–4 sections per mouse. Quantification of BACE1+ volume within 15 μm of X34+ amyloid plaque was done using Fiji (v3, ImageJ) by experimenters blind to genotype information. Thresholded X34 images were binarized and ROIs were automatically selected according to the X34 plaque area. ROIs were expanded using the expand function to 15 μm. BACE1 levels in wild type mice were determined by applying a X34-expanded mask belonging to a 5XFAD mouse to the same hippocampal region. BACE1 was measured after thresholding within the ROIs using the Analyze Particles function and was recorded as % area.

Synaptic mitochondrial isolation and Seahorse analysis

Synaptic mitochondria were isolated as described previously[40]. Briefly, brain cortices were removed and added to cold freshly prepared 9 ml of mitochondrial isolation buffer (IB; 225 mM mannitol, 75 mM sucrose, 2 mM K_2PO_4, 0.1% BSA, 5 mM HEPES, 1 mM EGTA (pH 7.2)). Tissues were homogenized using a dounce homogenizer. The resultant homogenate was centrifuged at 13,000g at 4°C and layered on top of 3 X 2-ml discontinuous gradient of 15%, 23% and 40% Percoll (GE) and centrifuged at 34,000g for 14 minutes at 4°C. Following centrifugation, the band between 15% and 23% containing synaptosomes and band between 23% and 40% containing nonsynaptic mitochondria were removed and washed in IB with 0.02% digitonin (for synaptosomes only). The isolates were then pelleted by centrifugation at 16,500g for 15 minutes at 4°C. The pellets were resuspended in IB and layered over another discontinuous gradient similar to that described above. Bands between 23% and 40% containing synaptic mitochondria were obtained and washed in ice cold IB. Protein estimation was performed using the Bradford assay (BioRad Laboratories). Isolated mitochondria were immediately used for Seahorse analysis to measure Complex II-mediated electron transport using the substrate succinate. 10 ug of freshly isolated synaptic mitochondria were plated in XFe24 cell culture microplates in a volume of 50ul mitochondrial assay solution (MAS; 70 mM Sucrose, 220 mM mannitol, 10 mM KH_2PO_4, 5 mM $MgCl_2$, 2 mM HEPES, 1 mM EGTA and 0.2% BSA with 10 mM succinate and 2 uM rotenone) and attached to the wells by spinning down the plates at 2000 rpm at 4°C. After attaching mitochondria to the plate wells, volume was brought up to 450 uL of MAS containing substrate. In the meantime, the Seahorse XF24 Flux Analyzer was equilibrated to 37°C overnight a day before the assay. The final concentrations of substrates and inhibitors added to the wells were 4 mM ADP, 2.5 μg/ml Oligomycin A, 4 μM FCCP and 4 μM Antimycin A. The coupling assays were run in 4–5 replicate wells for each independent biological sample. XF24 data were collected according to Seahorse software (Agilent).

The basal OCR was determined in the presence of the incubation medium. The proton leak was determined after inhibition of mitochondrial ATP production by oligomycin, an inhibitor of the F0 F1 ATPase. The measurement of ATP production in the basal state was obtained from the decrease in respiration by inhibition of the ATP synthase with oligomycin. Then, the mitochondrial electron transport chain was stimulated maximally by the addition of the uncoupler FCCP. Finally, extra-mitochondrial respiration was estimated after the addition of the antimycin A and rotenone inhibitors of the complexes III and I, respectively. Coupling efficiency is the proportion of the oxygen consumed that drives ATP synthesis compared with that driving the proton leak and was calculated as the fraction of basal mitochondrial OCR used for ATP synthesis (ATP-linked OCR/basal OCR). Spare capacity is the capacity of the cell to respond to an energetic demand and was calculated as the difference between the maximal respiration and basal respiration.

In vivo [^{18}F]FDG PET/CT imaging

[^{18}F]FDG was obtained from the Cyclotron & Radiochemistry Facility at Stanford University. Quality control criteria were set and the tests were performed according to USP 823. In vivo [^{18}F]FDG PET/CT imaging was performed in 17–19 mo female mice. Mice were fasted overnight (12–14h) prior to imaging with access to water. Mice were

anesthetized with isoflurane gas (2–3% in O_2) and blood samples acquired via tail prick were used to measure blood glucose levels in duplicates using a glucose meter (Accu-check) immediately prior to intraperitoneal injection with 292–322μCi of [^{18}F]FDG. Each mouse was anesthetized for a maximum of 5 minutes before being returned to home cage to allow tracer accumulation while awake. For PET/CT imaging, mice were anesthetized (3% for induction and 2% for maintenance in O_2) and 20 min static PET images were acquired at 75–95 min following [^{18}F]FDG injection using a dual microPET/CT scanner (Inveon, Siemens). A 3-dimensional ordered subsets expectation-maximum (3DOSEM, 2 iterations) and MAP-SP (18 iterations) reconstruction algorithm was applied to PET images (128 × 128 × 159 matrix size, 0.776 × 0.776 × 0.96mm voxel size). CT images were acquired to provide anatomical reference and to apply scatter and attenuation correction to PET data. PET images were analyzed using Vivoquant software (v3, inviCRO) and visualized using Inveon Research Workspace 3.0 (IRW, Siemens). Brain uptake was quantified as previously described using a brain atlas approach[63]. In brief, CT images were used to fit a 3-dimensional mouse brain atlas and to obtain [^{18}F]FDG uptake values in *a priori* regions of interest including the hippocampus and thalamus. PET uptake was expressed as SUVglc using the average blood glucose measurement for each mouse.

Analysis of Mouse Cortical Aβ42 and Aβ40

Soluble and insoluble protein fractions were prepared from mouse brain tissue as described by Casali and Landreth [64]. Briefly, cortex was mechanically homogenized with ice-cold tissue homogenization buffer (THB; 2mM Tris (pH 7.4), 250 mM sucrose, 0.5 mM EDTA, 0.5 mM EGTA) containing protease inhibitors (P8340, Sigma-Aldrich, St. Louis, MO). A 0.4% diethylamine (DEA) solution in 100 mM NaCl was added and samples were centrifuged at 135,000 × g for 1 hour at 4°C. The resulting supernatant represented the DEA soluble fraction. The pellet was further extracted with the addition of ice-cold 95% formic acid (FA), sonication on ice and centrifugation at 109,000 × g for 1 hour at 4°C. The resulting supernatant was neutralized using FA neutralization buffer (1 M Tris, 0.5 M Na_2HPO_4, and 0.05% NaN_3 and this sample represented the FA insoluble fraction. Protein concentrations of each sample were determined using the Bradford assay (Cat#5000006, Bio-Rad, Hercules, CA). Aβ42 and Aβ40 were measured using the V-PLEX Aβ Peptide Panel 1 (6E10) kit from MesoScale Discovery (Cat# K15200G, Rockville, Maryland) following manufacturer's directions with DEA fractions measured neat while FA fractions were diluted 1/2 using the sample diluent provided.

Immunofluorescent staining of human brain

Free-floating frontal cortex ribbons from Alzheimer's disease and control donors were obtained from the Banner Institute, Arizona Study of Aging and Neurodegenerative Disorders and Brain and Body Donation Program. Antigen retrieval was performed for 1 hour at 37°C using 10 mM citrate buffer solution with 0.05% Tween 20 (pH 6.0). Sections were incubated with 10 μM X-34 to identify amyloid plaques. Sections were washed with PBS and then blocked in 10% normal donkey serum (NDS, Cat# 017–000-121, Jackson ImmunoResearch Laboratories, Inc., West Grove, PA) in PBS. Sections were then incubated overnight in rabbit polyclonal anti-TREM1 (Cat# 93717, Abcam, 1:150, 93717) and anti-Iba1 (Cat# ab5076, Abcam) in 5% NDS in PBS with 0.4% Tween. Tissue was washed and

then incubated in secondary antibody solution (1:1000) in 2% NSD in PBS-T. Sections were washed, mounted on glass slides and coverslipped with Prolong Gold aqueous mounting media (Cat# P36930, ThermoFisher, Waltham, MA). Confocal images were acquired from layers II-V of cortex using a Zeiss LSM 980 confocal microscope. For AD sections, z-stacks spanning 15 μm (optical slice of 0.5 μm) were acquired by centering on an X-34+ amyloid plaque. Fiji was used to threshold maximally z-projected X-34 channel images, close holes, and create region of interests (ROIs) spanning amyloid plaques. The Enlarge selection function was applied to enlarge amyloid plaque ROIs by 15 μm. TREM1+/Iba1+ cells within 15 μm of X-34 amyloid plaques were defined as plaque associated while cells outside of this distance were defined as non-plaque associated. Plaque ROIs derived from AD brain were applied to AD plaque-free areas and control tissue to define sampling area. TREM1+/Iba1+ cells were counted within these ROIs and defined as non-plaque associated. The total number of TREM1+/Iba+ cells was divided by the sampled area of each ROI and therefore presented as number of TREM1+/Iba1+ cells per mm^2.

Quantitative immunoblotting of human AD brain

Postmortem brain material was obtained from the Arizona Study of Aging and Neurodegenerative Disorders and Brain and Body Donation Program[65]. Ethical approval for the Arizona Study of Aging and Neurodegenerative Disorders and Brain and Body Donation Program was by Western Institutional Research Board, a Banner Health-designated Institutional Review Board. AD was defined as intermediate or high probability that dementia was due to AD according to NIA-Reagan criteria[66]. For immunoblot experiments, patients consisted of four groups stratified by Braak stage[67] including non-demented Braak I–II - zero to sparse plaques (n=12), non-AD demented Braak I–II - zero to sparse plaques (n=11), AD Braak III–IV- demented with moderate plaques (n=12), and AD Braak V–VI - demented with frequent plaques (n=12). We excluded cases with clinicopathologic evidence of Parkinson’s disease (defined as having two of the three cardinal clinical signs of resting tremor, muscular rigidity and bradykinesia, along with pigmented neuron loss and Lewy bodies in the substantia nigra), dementia with Lewy bodies[68], progressive supranuclear palsy[69], motor neuron disease (including amyotrophic lateral sclerosis, primary lateral sclerosis and motor neuron disease associated with frontotemporal lobar degeneration), corticobasal degeneration (defined by the classic H&E histopathology of achromatic, swollen neurons in the cerebral cortex and indistinct inclusions within pigmented neurons of the substantia nigra as well as abnormal, phosphorylated tau or Gallyas-positive astrocytic plaques in the cerebral cortex), Pick’s disease (defined as clinical dementia with tau or silver-stain positive Pick bodies within neurons of the cerebral cortex, hippocampus and/or basal ganglia), multiple system atrophy (defined by atrophy and gliosis of the cerebellar folia, basal pons, substantia nigra and/or striatum, as well as alpha-synuclein or silver-positive glial and neuronal cytoplasmic inclusions), and Huntington’s disease (defined by the characteristic trinucleotide repeat expansion in the gene for huntingtin). Brains from subjects with cancer, sepsis, or stroke were also excluded. Post-mortem interval was less than 8 hours. Cases were balanced for sex in each group and all groups were matched for age at death. Demographic characteristics of the study participants are shown in Extended Data Table 2.

Frozen medial frontal gyrus (MFG) tissue was homogenized in 8x volume of lysis buffer (in 1% Triton X-100, 0.5% NP-40, 25 mM Tris HCl, 100 mM NaCl and protease and phosphatase inhibitors), sonicated, and centrifuged at 13,000 × g for 20 minutes. The protein concentration was determined using the BCA protein assay kit (Thermo Fisher Scientific, USA). Samples were separated on NuPAGE 4–12% Bis-Tris gels (Cat# WG1403A, Invitrogen) and transferred to polyvinylidene difluoride membranes (Cat# IPVH00010, Millipore Sigma, Burlington, MA). Membranes were blocked with Tris-buffered saline (TBS)/0.1% Tween-20/5% milk for 1 hour at room temperature (RT) and then incubated overnight at 4°C with primary antibodies against TREM1 (1:300; ab93717, Abcam, San Francisco, CA), β-Actin (1:10,000, A5441, Sigma-Aldrich, St. Louis, MO). Blots were washed 3 × 10 minutes with TBS-T and incubated for 2 hours with IRDye 800CW goat anti-rabbit (LI-COR Biosciences, Lincoln, NE) and IRDye 680RD goat anti-mouse (LI-COR Biosciences) secondary antibodies (both 1:10,000). Blots were imaged using a LI-COR CLX-1306 instrument and analysis was completed using Image Studio Lite software (Version 5.2.5, LI-COR Biosciences). Human liver tissue lysate (Cat# HT-314, Zyagen, San Diego, CA) was used as positive control for human TREM1 and TREM2 proteins. Positive controls and full uncropped blots are presented in Extended Data Fig. 8b–c and Supplemental Fig. 1.

Mendelian Randomization

Two-sample Mendelian randomization (MR) was used to infer the causal effect of sTREM1 and sTREM2 on AD risk using the TwoSampleMR package[70,71] with summary statistics from genome-wide association studies (GWAS) testing association with SomaScan aptamers level in 35,559 Icelanders[50] and with AD in 75,024 cases and 397,844 controls[51]. MR inverse variance weighting was used to assess the significance of the association of the exposure with the outcome. MR Egger and MR Median Weighted estimators were used to confirm the robustness of these associations. Bidirectional MR was used to confirm the direction of causality.

Statistics & Reproducibility

The sample sizes in the present study are similar to those reported in these previous publications. No power analyses were used to predetermine sample sizes. However, sample sizes were informed by prior literature using similar experimental paradigms that yielded interpretable results and the lab's previous experience[18,21,29,30,40,47,72–74]. Cells were pooled and randomly divided between vehicle controls and treated group for in vitro experiments. Animals were randomly assigned to treatment and control groups. Investigators were blind to group allocation during data collection and analysis. Means of two groups were compared using unpaired Student's *t*-tests. Pearson chi-square was used to compare differences in categorical variables. Normally distributed continuous variables were compared using one- and two-way ANOVA and Tukey's post hoc test. Non-normally distributed data were analyzed using nonparametric Kruskal-Wallis test followed by Dunn's multiple comparisons test. All tests were two-sided. Human TREM1 and TREM2 levels were analyzed by ANCOVA with age and sex included in the model. Associations between TREM1 and TREM2 with pathological features were analyzed using linear regression with age and sex included as predictors. Microsoft Excel v16.75 was used to collate data. The

statistical software packages used include R v.3.6.2 and Prism 8 and 9 (GraphPad Software). All data are presented as mean ± SEM unless otherwise noted.

Extended Data

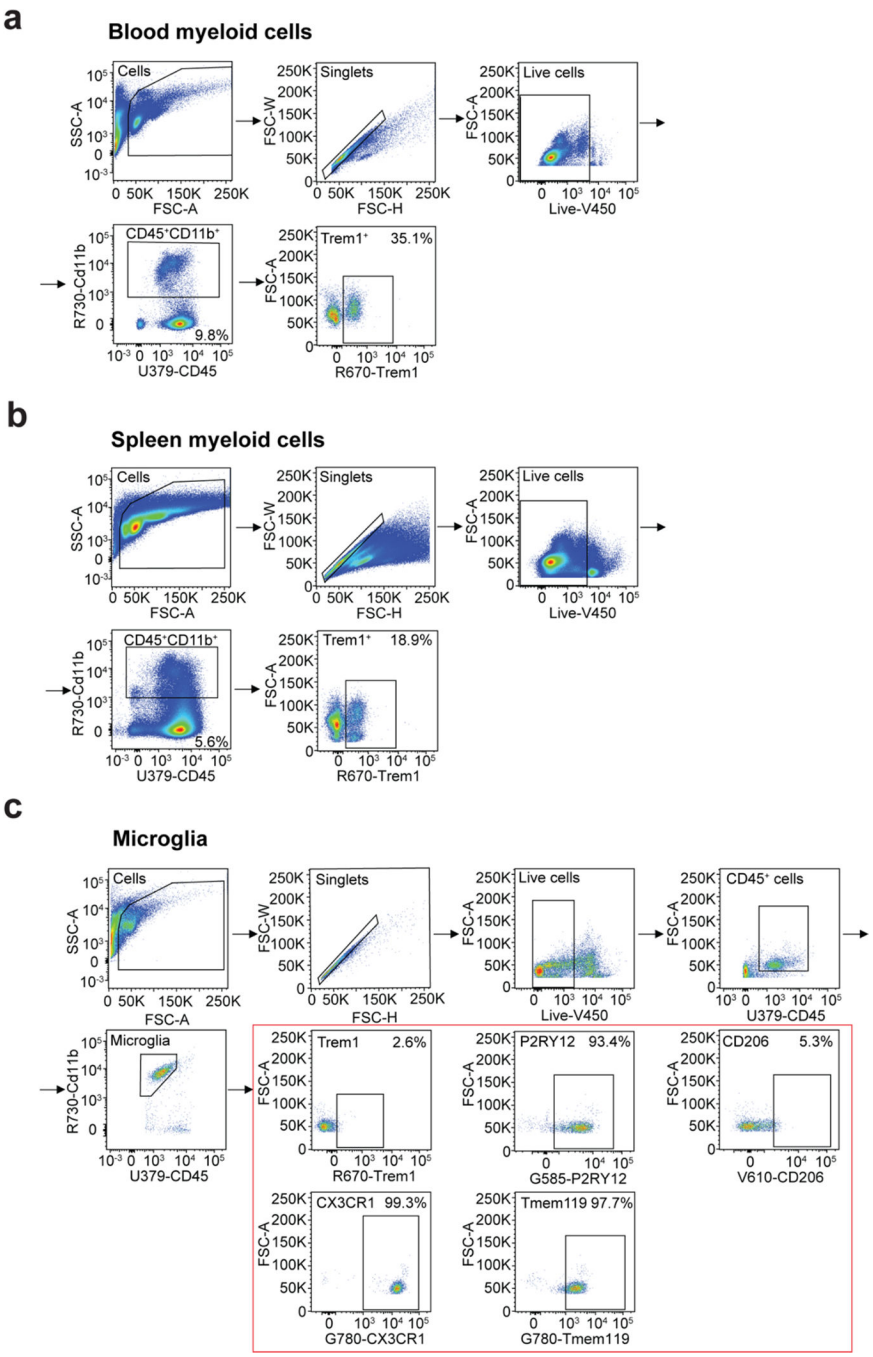

Extended Data Fig. 1. low cytometry gating for quantification of TREM1 expression in blood, spleen and brain myeloid cells

a. Gating strategy for live CD45+Cd11b+TREM1+ blood myeloid cells

b. Gating strategy for live CD45+Cd11b+TREM1+ spleen myeloid cells

c. Gating strategy for live CD45loCd11b+TREM1+ microglia; also includes gating for P2RY12, CD206, CX3CR1 and Tmem119 microglial markers.

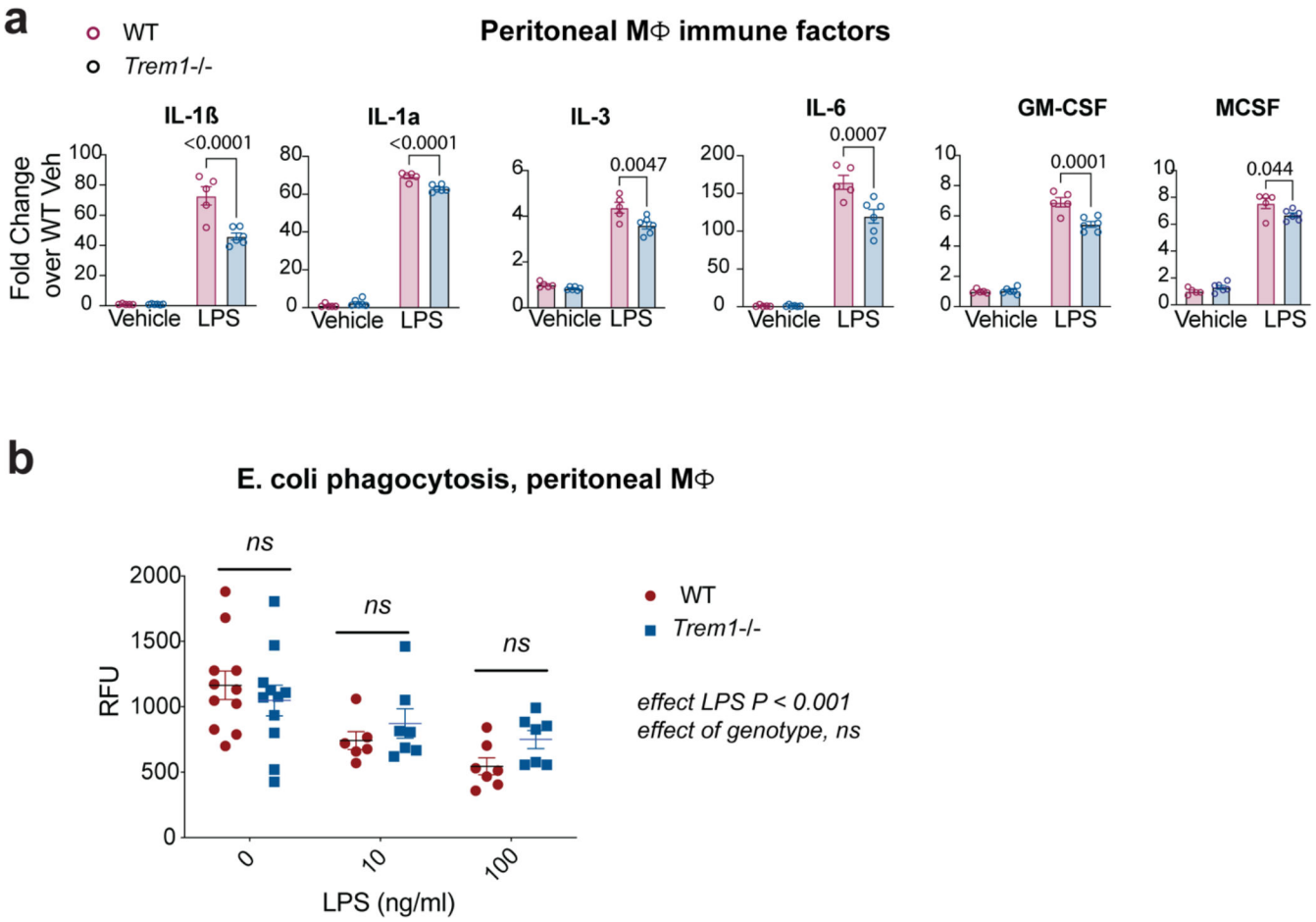

Extended Data Fig. 2. TREM1 amplifies levels of inflammatory factors but does not alter phagocytosis

Data are mean ±} s.e.m. unless otherwise indicated.

a. Quantification of immune factors in lysates of peritoneal MF isolated from 8.5 mo WT and Trem1−/− mice treated with vehicle or 100 ng/ml LPS for 20 hr. Two-way ANOVA with Tukey's multiple comparisons shown for WT+LPS vs Trem1−/−+ LPS (n=5–6 male mice per genotype as shown).

b. Trem1 deficiency does not alter phagocytosis in peritoneal MF. Cells were stimulated with vehicle or E.coli +/− LPS 100 ng/ml for 20h. 2-way ANOVA, effect of LPS ***P < 0.001, no effect of Trem1 genotype basally or with LPS stimulation. 2–3 mo male mice with 6–11 technical replicate wells as shown.

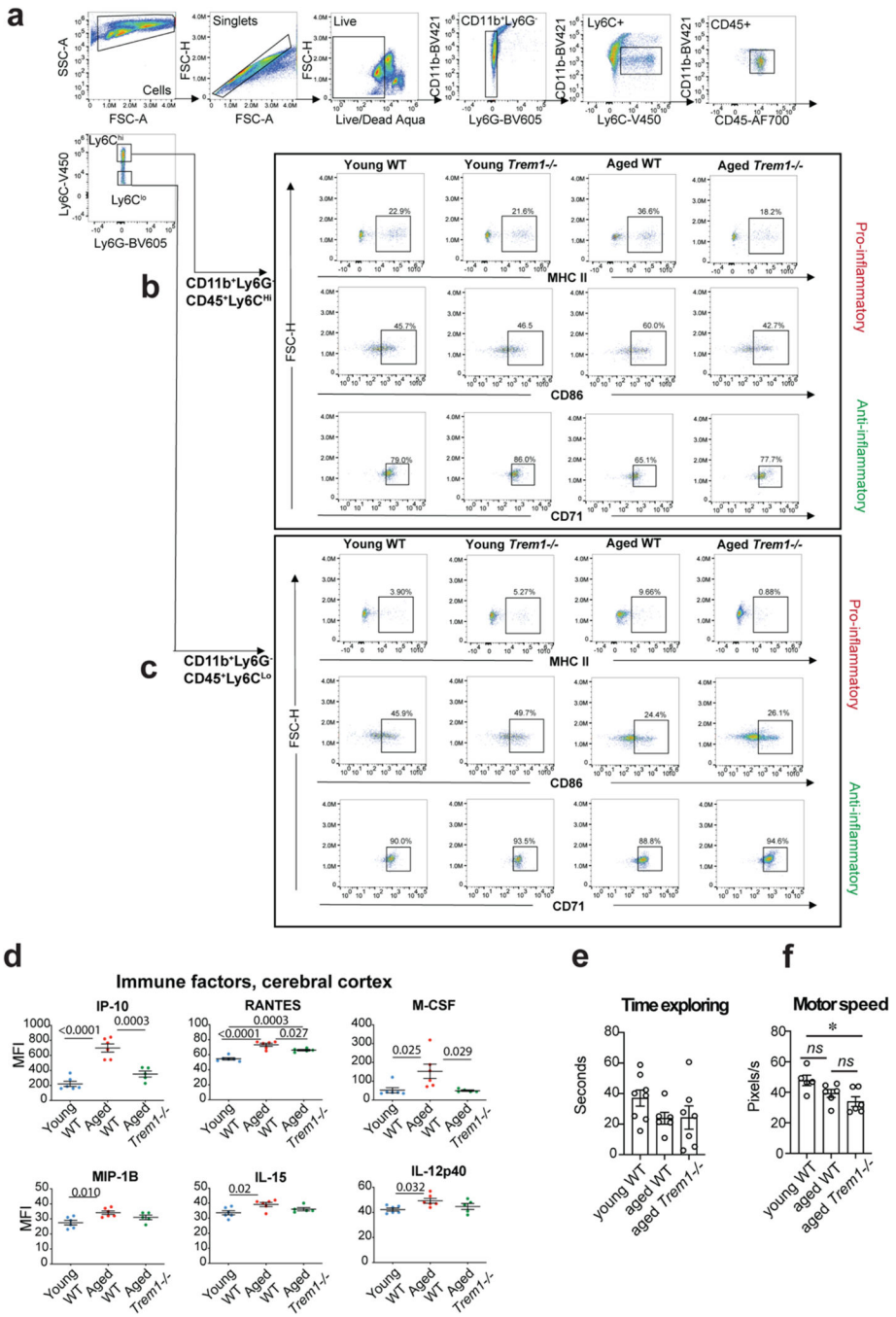

Extended Data Fig. 3. TREM1 promotes a pro-inflammatory polarization state in aged peritoneal MF

Data are mean ±} s.e.m. unless otherwise indicated.

a. Gating strategy for live Cd11b+Ly6G-CD45+Ly6CHi and Cd11b+Ly6G-CD45+Ly6CLo peritoneal MF from young WT and Trem1−/− (2 mo) and aged WT and Trem1−/− (22–23 mo) male mice.

b. Representative gating for MHC II, CD86, and CD71 positive Ly6CHi peritoneal MF.

c. Representative gating for MHC II, CD86, and CD71 positive Ly6CLo peritoneal MF.

d. Multianalyte Luminex quantification of immune factors in young WT (2 mo) and aged WT (23–24 mo) and aged Trem1−/− (23–24 mo) cerebral cortex. One-way ANOVA with Tukey's multiple comparisons shown (n=5–6 male mice per group as shown).

e. Total time exploring (in seconds) during the training phase of the NOR task; ANOVA with Tukey's multiple comparisons show no significant differences (n=6–8 female mice as shown).

f. Speed (pixels/second) of mice during the final trial of the Barnes Maze; ANOVA with Tukey's multiple comparisons (n=5–6 male and female mice as shown).

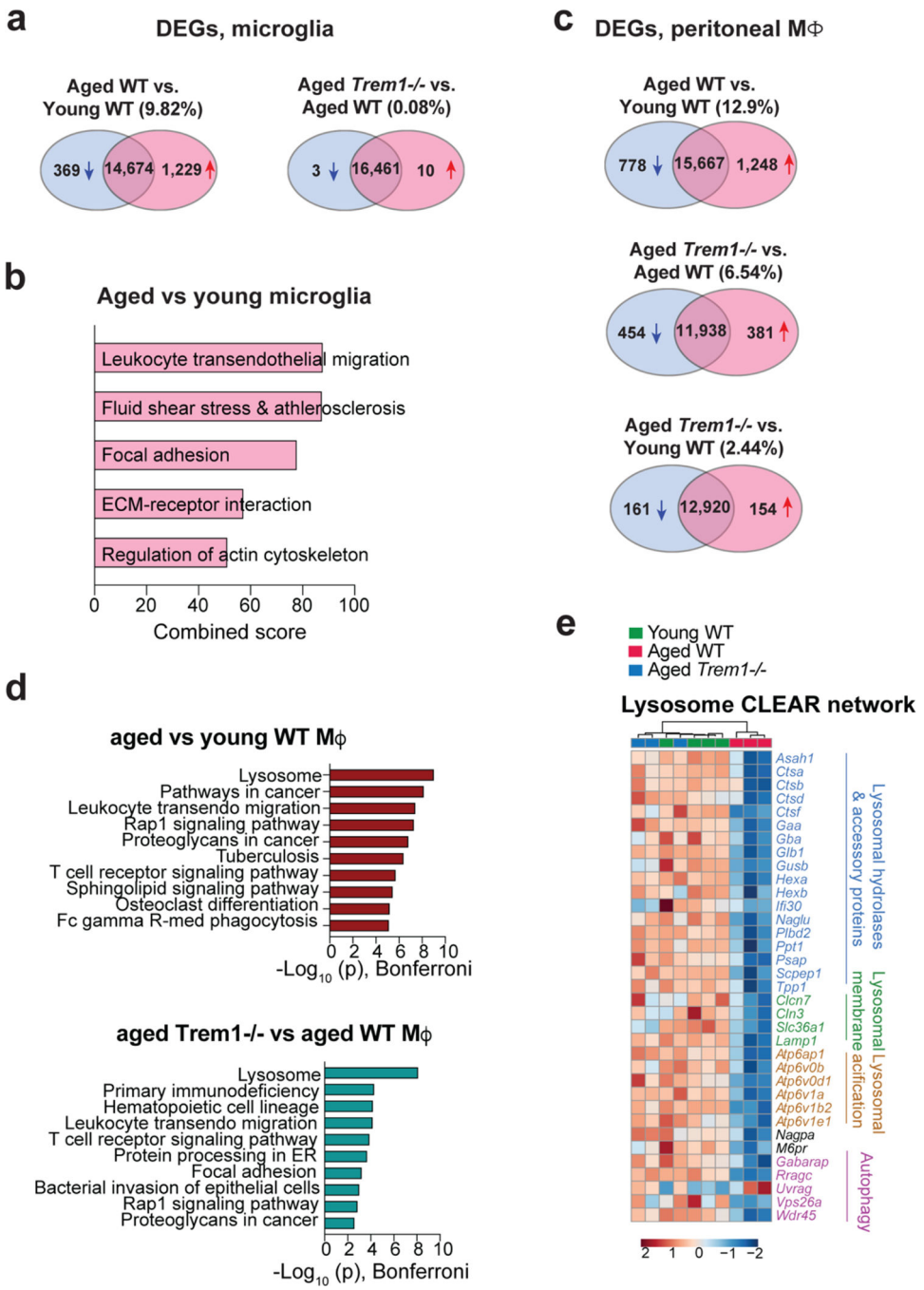

Extended Data Fig. 4. Trem1 deficiency alters gene expression in aged peripheral MF with minimal changes in aged brain microglia

a. Venn diagram of DEGs (all genes q < 0.05) in pairwise comparisons of microglia isolated from aged (18 – 20 mo) vs young (3 mo) mice and pairwise comparisons of microglia isolated from aged Trem1−/− vs aged WT mice (18–20 mo). Blue indicates number of downregulated genes while red indicates the number of upregulated genes (n=3 microglial samples (2 pooled male mice per sample) per group).

b. KEGG Pathway enrichment analysis of upregulated genes in aged compared to young microglia; there were no enriched pathways in the comparison of aged WT vs aged Trem1−/− microglia.

c. Venn diagrams showing the number of DEGs (all genes $q < 0.05$) in pairwise comparisons of primary mouse MF from young WT (2 mo), aged WT (25 mo) and aged Trem1−/− (25 mo) mice. Blue indicates number of downregulated genes while red indicates the number of upregulated genes (n=3–4 male mice per group).

d. Pathway enrichment analysis of upregulated genes in aged MF vs young and in aged Trem1−/− vs aged WT MF.

e. Heatmap of DEGs ($q < 0.05$) comprising the Coordinated Lysosomal Expression and Regulation (CLEAR) network. Lysosomal functional categories are indicated for each gene. Aged Trem1−/− mice cluster with the young WT mice. Scale represents z-score values from FPKM. n=3–4 male mice per group.

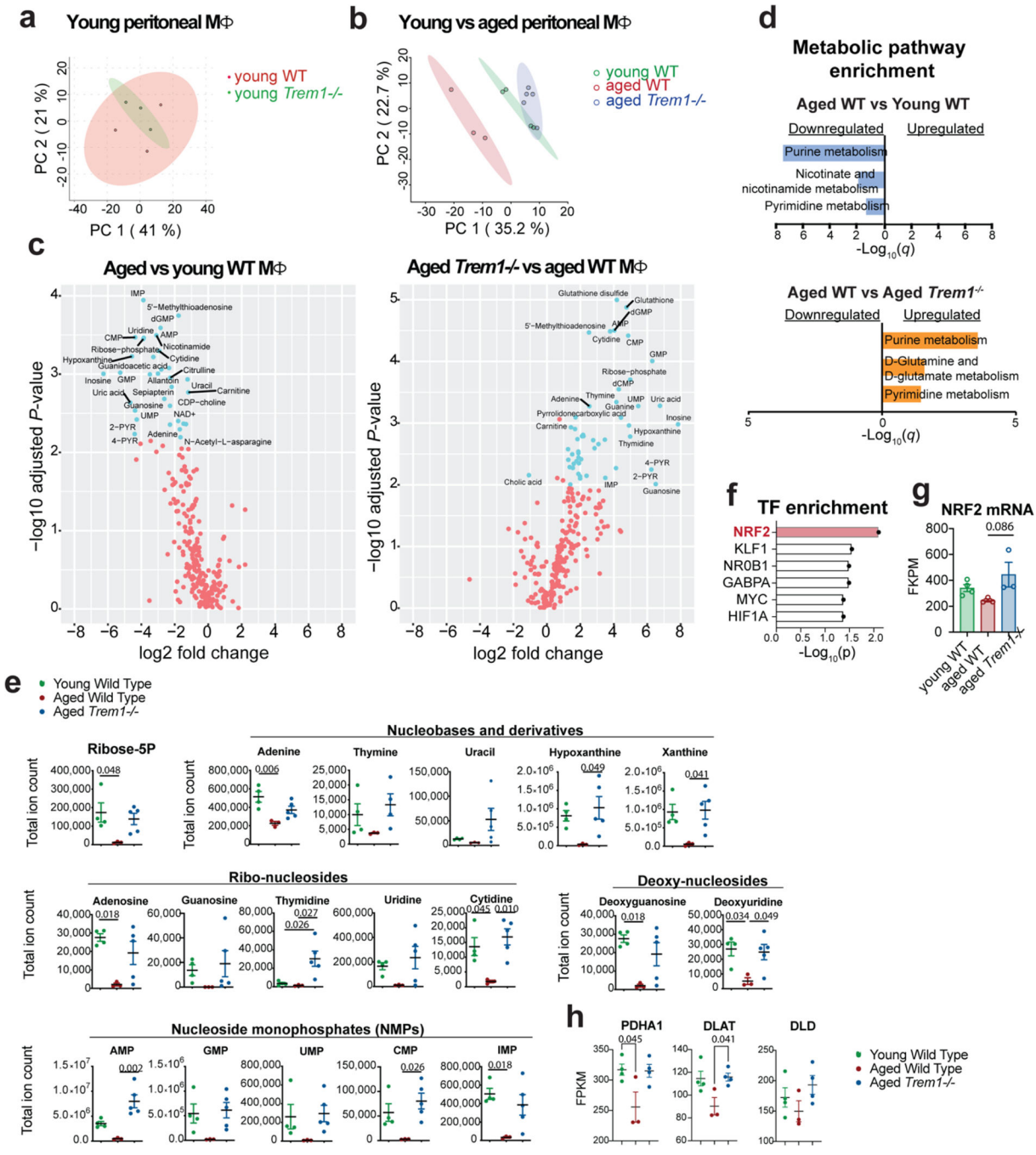

Extended Data Fig. 5. TREM1 deficiency restores youthful metabolism in aged macrophages
Data are mean ±} s.e.m. unless otherwise indicated.

a. PCA of metabolites from young (2 mo) WT and Trem1−/− peritoneal MF (n=3 male mice per group).

b. PCA of significantly regulated metabolites from primary peritoneal MF isolated from young WT (2mo), aged WT (25 mo) and aged Trem1−/− (25 mo) male mice. n=3–5 male mice per group.

c. Volcano plot comparing aged WT vs young WT (left) and aged Trem1−/− vs aged WT (right) peritoneal MF with Log2 fold change (FC) and -Log10(P) values of metabolites. Significantly regulated metabolites with -log10(P) > 2 and log2 fold change > 1 are shown in blue.

d. KEGG metabolic pathway enrichment analysis of differentially regulated metabolites between aged WT and young WT macrophages and between aged Trem1−/− vs aged WT MF. X-axis shows -Log10(q) value. No pathways were significant following FDR correction for the comparison of aged Trem1−/− vs young WT. Pathway analysis was performed using MetaboAnalyst 5.0; n=3–5 male mice per group.

e. Total ion count of Ribose-5P, the precursor of purines and pyrimidines and total ion counts for nucleobases and derivatives, ribo-nucleosides, deoxynucleosides, and nucleoside monophosphates. Data are analyzed by one-way ANOVA with Tukey's multiple comparisons (n=3–5 male mice per group). Abbreviations: AMP: adenosine monophosphate, GMP: guanosine monophosphate, UMP: uridine monophosphate, CMP cytidine monophosphate, IMP: inosine monophosphate. n=3–5 male mice per group as shown.

f. Transcription factor (TF) enrichment analysis revealing TFs enriched for differentially expressed metabolite enzymes.

g. FKPM of NRF2. ANOVA followed by Tukey's multiple comparison (n=3–4 male mice per group as shown).

h. FKPM of the 3 pyruvate dehydrogenase complex (PDH) subunits: pyruvate dehydrogenase (PDHA1), dihydrolipoyl transacetylase (DLAT) and dihydrolipoyl dehydrogenase (DLD); one-way ANOVA followed by Tukey's multiple comparison (n=3–4 male mice per group as shown).

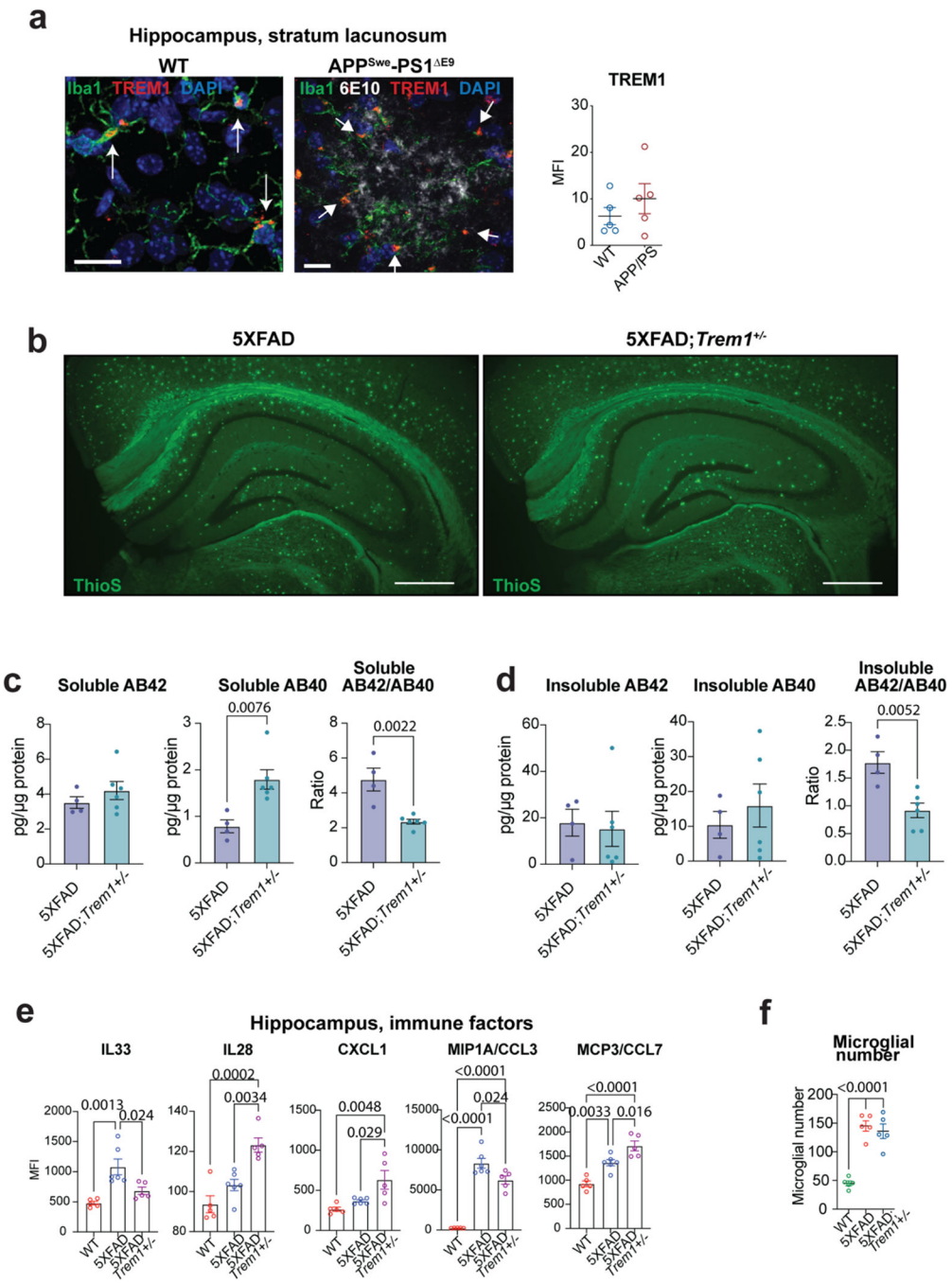

Extended Data Fig. 6. TREM1 expression does not significantly change in context of accumulating amyloid.

Data are mean ±} s.e.m. unless otherwise indicated.

a. (Left) Immunofluorescent staining of TREM1 in 9 mo WT and APPSwe-PS1ΔE9 hippocampal stratum lacunosum in IBA1+microglia. 5–7 hippocampal sections per mouse were imaged, n=5 10 male mice/genotype. Scale bar = 10 µm. TREM1 colocalizes with Iba1+ cells (white arrows). (Right) Quantification of MFI.

b. Thioflavin-S (ThioS) fluorescent staining of hippocampus in 9–10 mo 5XFAD and 5XFAD;Trem1+/− female mice. Scale bar = 500 μm.

c. Soluble levels of cerebral cortical As40 and 42 and the ratio of As42/40 in 5X FAD and 5XFAD;Trem1+/− mice. Student's two tailed t-test (n=4–6 males/group as shown, 10–13 mo)

d. Insoluble levels of cerebral cortical As40 and 42 and the ratio of As42/40 in 5X FAD and 5XFAD;Trem1+/− mice; Student's two tailed t-test (n=4–6 males/group as shown, 10–13 mo)

e. Quantification of hippocampal immune factors in WT, 5XFAD, and 5XFAD;Trem1+/− 10 mo mice. One-way ANOVA with Tukey post-hoc comparisons (n= 5–6 female mice per group as shown).

f. Microglial number from Fig. 4i. One-way ANOVA with Tukey's multiple comparisons (n=5 male mice per condition).

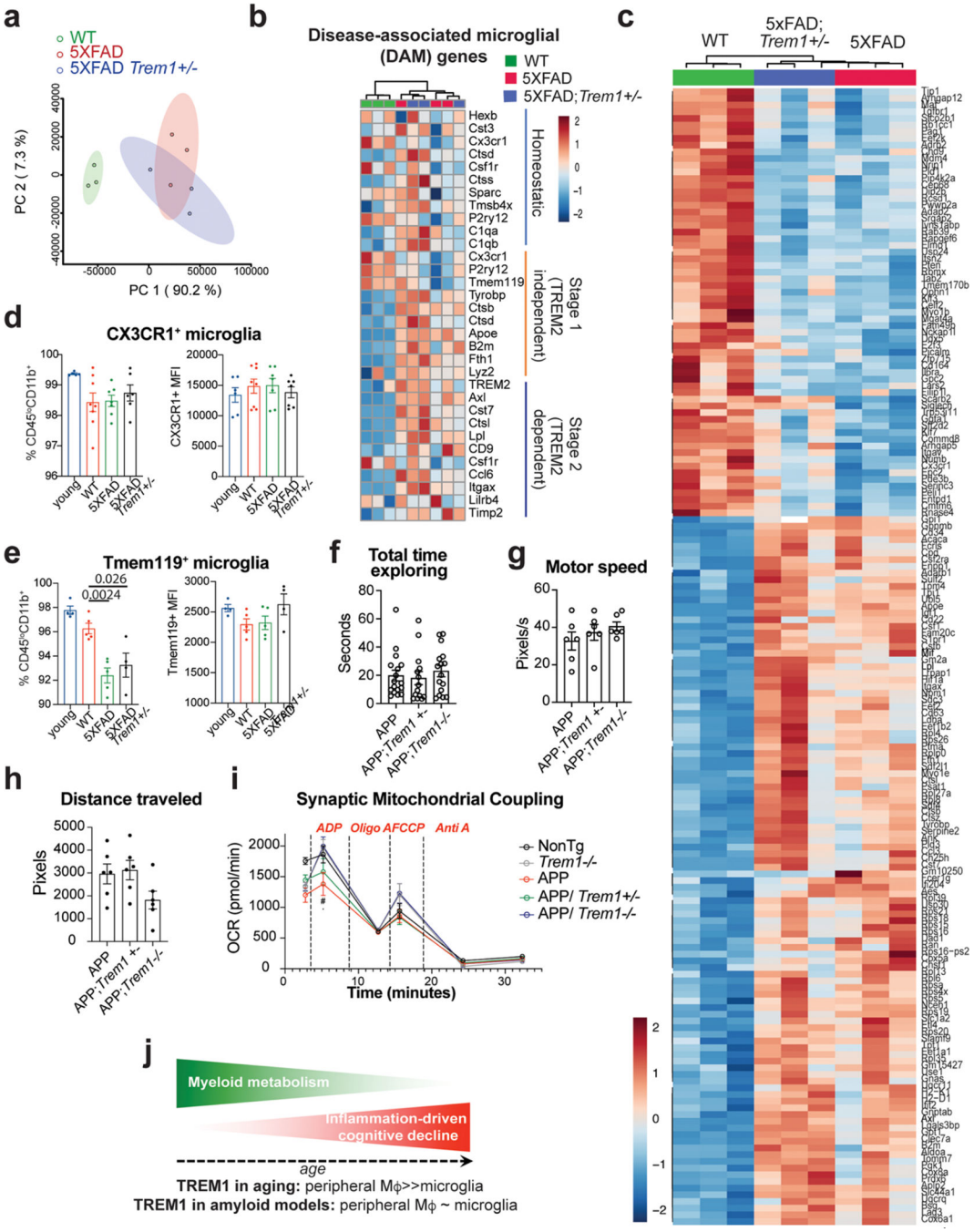

Extended Data Fig. 7. Disease-associated microglial (DAM) signature in 5XFAD;Trem1+/− mice.
Data are mean ±} s.e.m. unless otherwise indicated.

a. PCA of significantly regulated DAM signature genes from primary microglia isolated from WT, 5XFAD and 5XFAD/Trem1+/− mice. Individual microglial samples were pooled from 2 male mice (n=3 samples per condition).

b. Hierarchical clustering of DAM signature gene set showing homeostatic, DAM Stage 1 and DAM Stage 2 genes. Scale represents z-score values from FPKM.

c. Hierarchical clustering of top 170 DEGs (FDR-corrected) belonging to the full DAM signature gene set. Scale represents z-score values from FPKM. Scale represents z-score values from FPKM.

d. (Left) Percent of CX3CR1+ microglia in young (3 mo) and 13–17 mo WT, 5xFAD and 5xFAD;Trem1+/− mice. (Right) MFI of CX3CR1+ microglia. One-way ANOVA with Tukey's multiple comparison, not significant (n= 5–8 male and female mice per group as shown).

e. (Left) Percent of Tmem119+ microglia in young (3 mo) and 13–17 mo WT, 5xFAD and 5xFAD;Trem1+/− mice. (Right) MFI of Tmem119+ microglia. One-way ANOVA with Tukey's multiple comparisons (n=4–5 mice per group).

f. (Left) Total time exploring (in seconds) during the training phase of the NOR task in APPSwe mice; ANOVA with Tukey's post-hoc test (n=14–17 male and female mice per condition as shown).

g. Motor speed (pixels/sec) during the final training session of the Barnes maze; ANOVA with Tukey's post-hoc test (n=6 male and female mice per group).

h. Distance traveled during the final training session of the Barnes maze; ANOVA with Tukey's post-hoc test (n=6 male and female mice per group).

i. Coupling assay tracings of synaptic mitochondria oxygen consumption rates (OCR). Shown over time are the rates of basal Complex II respiration, State III (ADP stimulated respiration), State IV (oligomycin) and State IIIu (State III uncoupled, FCCP) that were consecutively measured over the course of the assay (n=5–9 male mice per condition).

j. Diagram of model of action of TREM1 in aging and transgenic mice with amyloid accumulation. In aging, peripheral TREM1 activity contributes to declines in myeloid metabolism and immune functions that lead to age-dependent cognitive decline. In models of amyloid accumulation, both peripheral and microglial TREM1 contribute to cognitive deficits associated with local accumulation of amyloid.

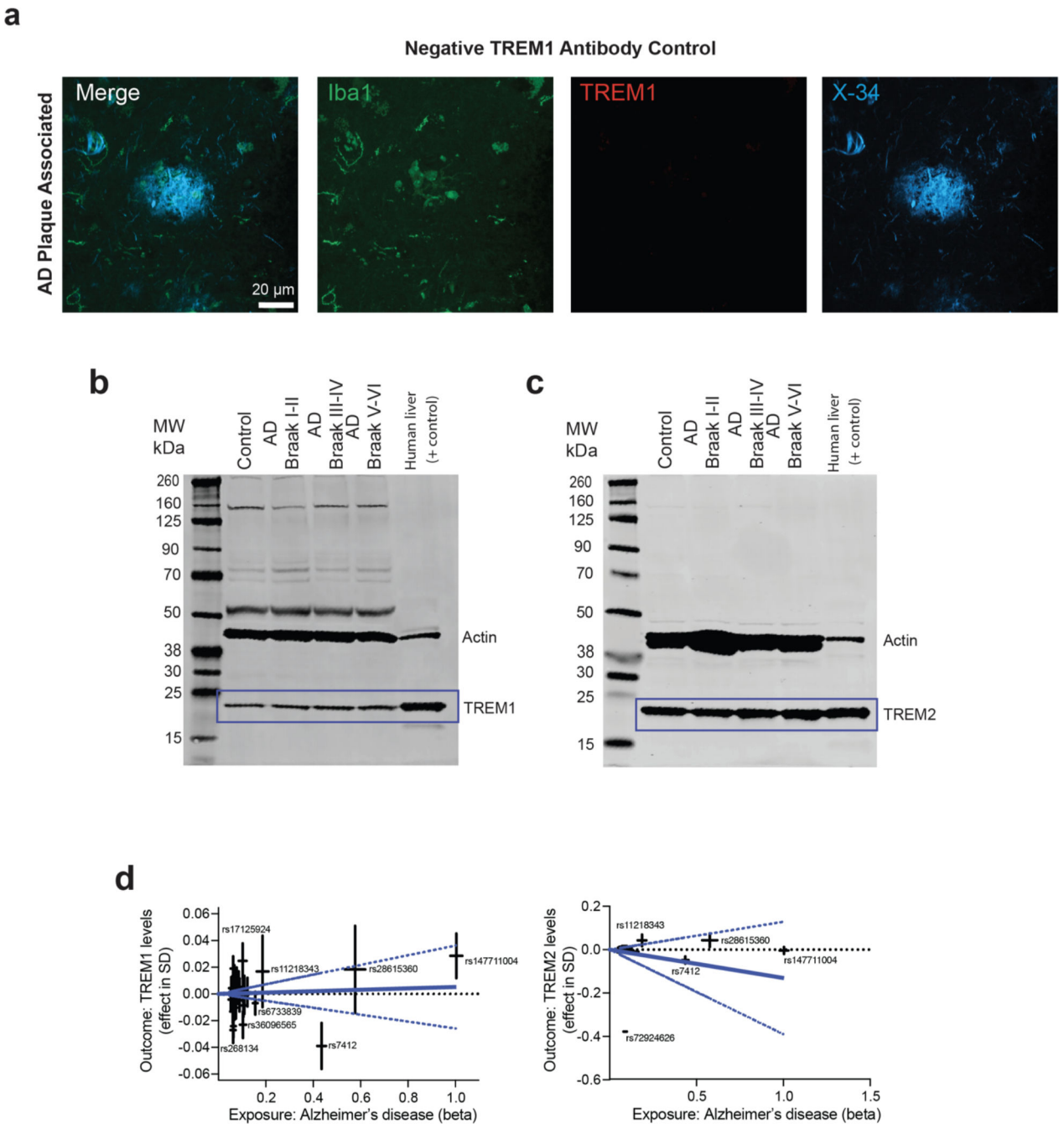

Extended Data Fig. 8. TREM1 expression in development of AD

a. Immunofluorescent staining of human frontal cortex without addition of TREM1 antibody and secondary only control (red), Iba1 (green), and X-34 (blue) signal. This antibody validation experiment was performed three times. Scale bar = 20 µm.

b. Immunoblot of TREM1 protein in postmortem human mid frontal gyrus. Clinicopathological diagnoses: non-demented Braak I-II, demented non-AD Braak stages I-II, AD Braak III-IV and AD Braak V-VI. Primary antibody detected human TREM1 band at the molecular weight of positive control (human liver lysates, Cat# HT-314, Zyagen, San

Diego, CA). The TREM1 band used for analysis are indicated by blue box. Also shown is the band for s-actin at 42 kDa. This antibody validation experiment was performed once.
c. Immunoblot of TREM2 protein in postmortem human mid frontal gyrus. Primary antibody detects human TREM2 band at the molecular weight of positive control (human liver lysates, Cat# HT-314, Zyagen, San Diego, CA). TREM2 bands used for analysis are indicated by blue box. Also shown is the band for s-actin at 42kDa. This antibody validation experiment was performed once.
d. Mendelian Randomization (MR) analyses with Alzheimer's disease (AD) risk level as exposure and sTREM1 plasma protein level as outcome. Blue lines are estimated MR-median weight effects, and the dashed lines indicate the 95% confidence interval for the MR effects.
e. Mendelian Randomization (MR) analyses with AD risk level as exposure and TREM2 plasma protein levels as outcome. Blue lines are estimated MR-median weight effects, and the dashed lines indicate the 95% confidence interval for the MR effects.

Extended Data Table 1:

List of Metabolites Detected by LC-MS

Metabolite	CDP-choline	L-Aspartyl-L-phenylalanine
5-Methoxytryptamine	citrulline	Linoleic acid
1-Methyl-Histidine	creatine	lysine
1-Methyladenosine	Creatine phosphate	m-Coumaric acid
2-Furoylglycine	cytidine	Melatonin
2-Phenylbutyric acid	D-Fructose-6-phosphate	methionine
2-PY	D-glucosamine-1/6-phosphate	Methionine sulfoxide
2-PYR	deoxyadenosine	N-Acetyl-L-alanine
3-Hydroxyanthranilic acid	deoxyguanosine	N-Acetyl-L-arginine
3-Methyl-Histidine	deoxyuridine	N-Acetyl-L-asparagine
4-Guanidinobutanoic acid	dGDP	N-acetyl-L-glutamine
4-PY	dGMP	N-Acetyl-L-isoleucine
4-PYR	DL-2-Aminooctanoic acid	N-Acetyl-L-leucine
4-Trimethylammoniobutanal	FAD	N-Acetyl-L-proline
5-Methoxytryptophan	GDP	N-Acetylcarnitine
5-Phenylvaleric acid	glucosamine-6-phosphate	N-Acetyllysine
5'-Methylthioadenosine	glucose-1 -phosphate	N-Acetylserine
acetyl-CoA	glutamate	N-Acetylserotonin
adenine	glutamine	N-Octanoylglycine
adenosine	GMP	NAD+
ADP	GSH:GSSG	NADP+
Aminoadipic acid	guanine	NADPH
AMP	histidine	NaR
Anserine	hydroxyproline	1-Methyl imidozolacetic acid hydrochloride
anthranilate	IDP	2-Amino-3-phosphonopropionic acid
arginine	Imidazoleacetic acid	2-Furoylglycine

aspartate	IMP	2-Hydroxybutyric acid
ATP	Indole-3-ethanol	2-Methyl-3-ketovaleric acid
carnitine	inosine	2-Phenylbutyric acid
Carnosine	kynurenic acid	2-PY
CDP	kynurenine	3-Cresotinic acid
3-Hydroxyanthranilic acid	Cholic acid	glycine
3-hydroxylbutyrate	citrate/isocitrate	glycolate
3-Methyladipic acid	CMP	Glycyl-L-leucine
4-PY	creatine	Glycyl-L-proline
5-Aminopentanoic acid	Creatine phosphate	Guanidoacetic acid
5-Hydroxymethyluracil	Creatinine	guanine
5-Phenylvaleric acid	D-2-Aminobutyric acid	guanosine
7-methylguanosine	D-erythrose-4-phosphate	histidine
a-ketoglutarate	D-Fructose-6-phosphate	Homocarnosine
acetoacetate	D-Phenyllactic acid	homoserine
acetylphosphate	D-Xylose	Hydroxyphenyllactic acid
aconitate	dCMP	hydroxyphenyl pyruvate
Aconitic acid	deoxyribose-phosphate	hydroxyproline
Adonitol	dGDP	hypoxanthine
ADP	dimethylglycine	IDP
ADP-D-glucose	Dimethylmalonic acid	IMP
alanine	DL-Valine	isoleucine
allantoin	FAD	L-2-Hydroxyglutaric acid
Alloisoleucine	Fructose	lactate
Aminoadipic acid	fructose-1–6-bisphosphate	Lactose
Aminolevulinic acid	fumarate	leucine
Anserine	Galactose	Linoleic acid
anthranilate	Galacturonic acid	lysine
Arachidic acid	GDP	m-Coumaric acid
arginine	Glucose	malate
asparagine	glucose-1 -phosphate	Malonic acid
aspartate	glutamate	Mandelic acid
ATP	glutamine	methionine
b-alanine	Glutaric acid	Methionine sulfoxide
b-Aminoisobutyric acid	glutathione	Methylglutaric acid
betaine	glutathione disulfide	Methylmalonic acid
Carnosine	Glyceraldehyde-3-phosphate	Methyloxovaleric acid (Ketoleucine)
CDP	glycerate	Methylsuccinic acid
myo-inositol	serine	Retinal
Myristic acid	shikimate	Retinoic Acid
N-Acetyl-L-alanineneg	sn-glycerol-3-phosphate	ribose-phosphate
N-Acetyl-L-asparagine	Stearic acid	Ribothymidine
N-Acetyl-L-isoleucine	Suberic acid	taurine

N-Acetyl-L-leucine	succinate	Taurodeoxycholic acid
N-Acetylaspartic acid	Taurodeoxycholic acid	threonine
N-Acetylcarnitine	threonine	thymidine
N-Acetylglycine	thymine	thymine
N-Methyl-D-aspartic acid	Tiglic acid	Tryptamine
N-Octanoylglycine	trans-Glutaconic acid	tryptophan
NAD+	tryptophan	UDP
nicotinamide	tyrosine	UMP
nicotinate	UDP	uridine
O-acetyl-L-serine	UDP-D-glucose	Xanthurenic acid
O-Phosphoethanolamine	Undecanoic acid	
ornithine	uracil	
orotate	Uric acid	
p-Cresol	uridine	
pantothenate	Urocanic acid	
Parahydroxyphenylacetic acid	valine	
phenylalanine	xanthine	
phosphoenol pyruvate	nicotinamide	
Pimelic acid	nicotinamide mononucleotide	
proline	nicotinamide riboside-2	
Pyroglutamic acid	O-acetyl-L-serine	
Pyrrolidonecarboxylic acid	O-Phosphoethanolamine	
pyruvate	ornithine	
quinolinate	pantothenate	
Retinal	phenylalanine	
Retinoic Acid	Pipecolic acid	
sarcosine	Pyroglutamic acid	
Sepiapterin	Pyrrolidonecarboxylic acid	

Extended Data Data Table 2:

Demographic Characteristics of Study Participants

Variable	Total (*n* = 48)	Non-Demented Braak I-II (*n*=12)	Demented Braak I-II (*n*=12)	AD Braak III-IV (*n*=12)	AD Braak V- VI (*n*=12)	*P*
Gender (F/M), no. (%)	23 (48)/25 (52)	5 (42)/7 (58)	6 (50)/6 (50)	6 (50)/6 (50)	6 (50)/6 (50)	ns, a
Age, years (mean +/− SD)	83.2 (4.1)	81.8 (4.1)	82.4 (4.0)	83.2 (4.3)	84.3 (3.9)	ns, b
PMI (hours)	3.14 (1.14)	2.95 (0.27)	3.38 (0.48)	3.24 (0.32)	2.99 (0.21)	ns, b
CERAD Neuritic Plaque Density (median, +/− SD)	2.5 (1.71)	1.5 (0.52)	2 (0.29)	4 (0.58)$	6 (0.51)&	*P*<0.0001, c
Braak Stage (median, +/− SD)	2.5 (0.99)	1 (0.83)	2 (0.45)#	3 (0.45)&	3 (0.00)&	*P*<0.0001, c

[a]Chi-Square test

[b] One Way ANOVA

[c] Kruskal-Wallis test, Dunn's multiple comparisons test

[#,] $P<0.05$ vs Non-Demented Braak I-II

[$,] $P<0.05$ vs Non-Demented Braak I-II

[&,] $P<0.0001$ vs Non-Demented Braak I-II

Supplementary Material

Refer to Web version on PubMed Central for supplementary material.

ACKNOWLEDGEMENTS

This work was supported by RF1AG053001K (KIA), RO1NS100180 (KIA), RF1AG070131 (KIA), RF1AG070839 (KIA), P30 AG0066515 (KIA), American Heart Foundation 19PABH1345800 (KIA), The Phil & Penny Knight Initiative for Brain Resilience at the Wu Tsai Neurosciences Institute, Stanford University (KIA), The Archer Foundation (KIA), Stanford School of Medicine Dean's Postdoctoral Fellowship (ENW and EB), HHMI Hanna H. Gray Fellows Program (MRM), Burroughs Wellcome Fund PDEP (MRM), Alzheimer's Association Research Fellowship (KAZ), The Paul and Daisy Soros Fellowship for New Americans (PSM), the Gerald J. Lieberman Fellowship (PSM), Marie Skłodowska-Curie Grant 888494 (EB). KIA is a Chan Zuckerberg-San Francisco Biohub Investigator. Data and tissue were obtained from the Arizona Study of Aging and Neurodegenerative Disorders (AZSAND) (www.brainandbodydonationprogram.org) supported by U24NS072026, P30AG19610, the Arizona Department of Health Services, the Arizona Biomedical Research Commission and the Michael J. Fox Foundation for Parkinson's Research. We are grateful to the Stanford Cyclotron & Radiochemistry Facility, the Stanford SCi3 Small-Animal Imaging Facility, the Stanford Shared FACS Facility, Stanford Human Immune Monitoring Core, and the Stanford Neuroscience Microscopy Service.

Data Availability

Source data are provided with this paper. The data discussed in this publication have been deposited in NCBI's Gene Expression Omnibus and are accessible through GEO Series accession number GSE229327 (https://www.ncbi.nlm.nih.gov/geo/query/acc.cgi?acc=GSE229327) for mouse macrophage transcript data and GSE229620 (https://www.ncbi.nlm.nih.gov/geo/query/acc.cgi?acc=GSE229620) for mouse microglia transcript data.

REFERENCES

1. Lindenberger U Human cognitive aging: corriger la fortune? Science 346, 572–578 (2014). 10.1126/science.1254403 [PubMed: 25359964]
2. Cunningham C & Hennessy E Co-morbidity and systemic inflammation as drivers of cognitive decline: new experimental models adopting a broader paradigm in dementia research. Alzheimers Res Ther 7, 33 (2015). 10.1186/s13195-015-0117-2 [PubMed: 25802557]
3. Franceschi C et al. Inflammaging and anti-inflammaging: a systemic perspective on aging and longevity emerged from studies in humans. Mech Ageing Dev 128, 92–105 (2007). 10.1016/j.mad.2006.11.016 [PubMed: 17116321]
4. Nikolich-Zugich J The twilight of immunity: emerging concepts in aging of the immune system. Nat Immunol 19, 10–19 (2018). 10.1038/s41590-017-0006-x [PubMed: 29242543]
5. Andrews SJ, Fulton-Howard B & Goate A Interpretation of risk loci from genome-wide association studies of Alzheimer's disease. Lancet Neurol 19, 326–335 (2020). 10.1016/s1474-4422(19)30435-1 [PubMed: 31986256]
6. Guerreiro R et al. TREM2 variants in Alzheimer's disease. N Engl J Med 368, 117–127 (2013). 10.1056/NEJMoa1211851 [PubMed: 23150934]
7. Cruchaga C et al. GWAS of cerebrospinal fluid tau levels identifies risk variants for Alzheimer's disease. Neuron 78, 256–268 (2013). 10.1016/j.neuron.2013.02.026 [PubMed: 23562540]

8. Jonsson T et al. Variant of TREM2 associated with the risk of Alzheimer's disease. The New England journal of medicine 368, 107–116 (2013). 10.1056/NEJMoa1211103 [PubMed: 23150908]
9. Melchior B et al. Dual induction of TREM2 and tolerance-related transcript, Tmem176b, in amyloid transgenic mice: implications for vaccine-based therapies for Alzheimer's disease. ASN Neuro 2, e00037 (2010). 10.1042/AN20100010 [PubMed: 20640189]
10. Leyns CEG et al. TREM2 function impedes tau seeding in neuritic plaques. Nat. Neurosci. 22, 1217–1222 (2019). 10.1038/s41593-019-0433-0 [PubMed: 31235932]
11. Wang Y et al. TREM2 lipid sensing sustains the microglial response in an Alzheimer's disease model. Cell 160, 1061–1071 (2015). 10.1016/j.cell.2015.01.049 [PubMed: 25728668]
12. Wang Y et al. TREM2-mediated early microglial response limits diffusion and toxicity of amyloid plaques. J Exp Med 213, 667–675 (2016). 10.1084/jem.20151948 [PubMed: 27091843]
13. Yuan P et al. TREM2 Haplodeficiency in Mice and Humans Impairs the Microglia Barrier Function Leading to Decreased Amyloid Compaction and Severe Axonal Dystrophy. Neuron 90, 724–739 (2016). 10.1016/j.neuron.2016.05.003 [PubMed: 27196974]
14. Song WM et al. Humanized TREM2 mice reveal microglia-intrinsic and -extrinsic effects of R47H polymorphism. J. Exp. Med. 215, 745–760 (2018). 10.1084/jem.20171529 [PubMed: 29321225]
15. Keren-Shaul H et al. A Unique Microglia Type Associated with Restricting Development of Alzheimer's Disease. Cell 169, 1276–1290.e1217 (2017). 10.1016/j.cell.2017.05.018 [PubMed: 28602351]
16. Boufenzer A et al. TREM-1 Mediates Inflammatory Injury and Cardiac Remodeling Following Myocardial Infarction. Circ. Res. 116, 1772–1782 (2015). 10.1161/CIRCRESAHA.116.305628 [PubMed: 25840803]
17. Knapp S et al. Cutting edge: expression patterns of surface and soluble triggering receptor expressed on myeloid cells-1 in human endotoxemia. J Immunol 173, 7131–7134 (2004). [PubMed: 15585833]
18. Liu Q et al. Peripheral TREM1 responses to brain and intestinal immunogens amplify stroke severity. Nat Immunol 20, 1023–1034 (2019). 10.1038/s41590-019-0421-2 [PubMed: 31263278]
19. Gibot S et al. A soluble form of the triggering receptor expressed on myeloid cells-1 modulates the inflammatory response in murine sepsis. J Exp Med 200, 1419–1426 (2004). 10.1084/jem.20040708 [PubMed: 15557347]
20. Gibot S et al. Plasma level of a triggering receptor expressed on myeloid cells-1: its diagnostic accuracy in patients with suspected sepsis. Ann Intern Med 141, 9–15 (2004). [PubMed: 15238365]
21. Chaney AM et al. PET imaging of TREM1 identifies CNS-infiltrating myeloid cells in a mouse model of multiple sclerosis. Sci Transl Med 15, eabm6267 (2023). 10.1126/scitranslmed.abm6267 [PubMed: 37379371]
22. Colonna M TREMs in the immune system and beyond. Nature reviews. Immunology 3, 445–453 (2003). 10.1038/nri1106
23. Colonna M & Facchetti F TREM-1 (triggering receptor expressed on myeloid cells): a new player in acute inflammatory responses. J. Infect. Dis. 187 Suppl 2, S397–401 (2003). 10.1086/374754 [PubMed: 12792857]
24. Bouchon A, Dietrich J & Colonna M Cutting edge: inflammatory responses can be triggered by TREM-1, a novel receptor expressed on neutrophils and monocytes. J. Immunol. 164, 4991–4995 (2000). [PubMed: 10799849]
25. Netea MG et al. Triggering receptor expressed on myeloid cells-1 (TREM-1) amplifies the signals induced by the NACHT-LRR (NLR) pattern recognition receptors. J. Leukoc. Biol. 80, 1454–1461 (2006). 10.1189/jlb.1205758 [PubMed: 16940328]
26. Tammaro A et al. TREM-1 and its potential ligands in non-infectious diseases: from biology to clinical perspectives. Pharmacol. Ther. 177, 81–95 (2017). 10.1016/j.pharmthera.2017.02.043 [PubMed: 28245991]
27. Replogle JM et al. A TREM1 variant alters the accumulation of Alzheimer-related amyloid pathology. Ann. Neurol. 77, 469–477 (2015). 10.1002/ana.24337 [PubMed: 25545807]

28. Liu YS et al. Common Variant in TREM1 Influencing Brain Amyloid Deposition in Mild Cognitive Impairment and Alzheimer's Disease. Neurotox Res 37, 661–668 (2020). 10.1007/s12640-019-00105-y [PubMed: 31721052]
29. Minhas PS et al. Restoring metabolism of myeloid cells reverses cognitive decline in ageing. Nature 590, 122–128 (2021). 10.1038/s41586-020-03160-0 [PubMed: 33473210]
30. Minhas PS et al. Macrophage de novo NAD(+) synthesis specifies immune function in aging and inflammation. Nat Immunol 20, 50–63 (2019). 10.1038/s41590-018-0255-3 [PubMed: 30478397]
31. Flowers A, Bell-Temin H, Jalloh A, Stevens SM Jr. & Bickford PC Proteomic anaysis of aged microglia: shifts in transcription, bioenergetics, and nutrient response. J Neuroinflammation 14, 96 (2017). 10.1186/s12974-017-0840-7 [PubMed: 28468668]
32. Rath S et al. MitoCarta3.0: an updated mitochondrial proteome now with sub-organelle localization and pathway annotations. Nucleic Acids Res 49, D1541–D1547 (2021). 10.1093/nar/gkaa1011 [PubMed: 33174596]
33. Fox DB et al. NRF2 activation promotes the recurrence of dormant tumour cells through regulation of redox and nucleotide metabolism. Nat Metab 2, 318–334 (2020). 10.1038/s42255-020-0191-z [PubMed: 32691018]
34. Zhang H, Davies KJA & Forman HJ Oxidative stress response and Nrf2 signaling in aging. Free Radic. Biol. Med. 88, 314–336 (2015). 10.1016/j.freeradbiomed.2015.05.036 [PubMed: 26066302]
35. Lee WJ et al. Regional Aβ-tau interactions promote onset and acceleration of Alzheimer's disease tau spreading. Neuron 110, 1932–1943.e1935 (2022). 10.1016/j.neuron.2022.03.034 [PubMed: 35443153]
36. Oblak AL et al. Comprehensive Evaluation of the 5XFAD Mouse Model for Preclinical Testing Applications: A MODEL-AD Study. Frontiers in Aging Neuroscience 13 (2021). 10.3389/fnagi.2021.713726
37. Borchelt DR, Ratovitski T, van Lare J, Lee MK, Gonzales V, Jenkins NA, Copeland NG, Price DL, Sisodia SS Accelerated amyloid deposition in the brains of transgenic mice co-expressing mutant presenilin 1 and amyloid precursor protein. Neuron 19, 939–945 (1997). [PubMed: 9354339]
38. Jain N, Lewis CA, Ulrich JD & Holtzman DM Chronic TREM2 activation exacerbates Abeta-associated tau seeding and spreading. J. Exp. Med. 220 (2023). 10.1084/jem.20220654
39. Hsiao K et al. Correlative memory deficits, Abeta elevation, and amyloid plaques in transgenic mice. Science 274, 99–102 (1996). [PubMed: 8810256]
40. Gauba E, Chen H, Guo L & Du H Cyclophilin D deficiency attenuates mitochondrial F1Fo ATP synthase dysfunction via OSCP in Alzheimer's disease. Neurobiol. Dis. 121, 138–147 (2019). 10.1016/j.nbd.2018.09.020 [PubMed: 30266287]
41. Bouter C & Bouter Y (18)F-FDG-PET in Mouse Models of Alzheimer's Disease. Front Med (Lausanne) 6, 71 (2019). 10.3389/fmed.2019.00071 [PubMed: 31058151]
42. Braak H & Braak E Neuropathological stageing of Alzheimer-related changes. Acta Neuropathol 82, 239–259 (1991). [PubMed: 1759558]
43. Rajkowska G & Goldman-Rakic PS Cytoarchitectonic definition of prefrontal areas in the normal human cortex: II. Variability in locations of areas 9 and 46 and relationship to the Talairach Coordinate System. Cereb. Cortex 5, 323–337 (1995). 10.1093/cercor/5.4.323 [PubMed: 7580125]
44. Thompson PM et al. Cortical change in Alzheimer's disease detected with a disease-specific population-based brain atlas. Cereb. Cortex 11, 1–16 (2001). 10.1093/cercor/11.1.1 [PubMed: 11113031]
45. Clinton J, Blackman SE, Royston MC & Roberts GW Differential synaptic loss in the cortex in Alzheimer's disease: a study using archival material. Neuroreport 5, 497–500 (1994). 10.1097/00001756-199401120-00032 [PubMed: 8003683]
46. Edler MK, Mhatre-Winters I & Richardson JR Microglia in Aging and Alzheimer's Disease: A Comparative Species Review. Cells 10 (2021). 10.3390/cells10051138
47. Wilson EN et al. Soluble TREM2 is elevated in Parkinson's disease subgroups with elevated CSF tau. Brain 143, 932–943 (2020). [PubMed: 32065223]

48. Suarez-Calvet M et al. sTREM2 cerebrospinal fluid levels are a potential biomarker for microglia activity in early-stage Alzheimer's disease and associate with neuronal injury markers. EMBO Molecular Medicine 8, 466–476 (2016). 10.15252/emmm.201506123 [PubMed: 26941262]

49. Shi X, Wei T, Hu Y, Wang M & Tang Y The associations between plasma soluble Trem1 and neurological diseases: a Mendelian randomization study. J Neuroinflammation 19, 218 (2022). 10.1186/s12974-022-02582-z [PubMed: 36068612]

50. Ferkingstad E et al. Large-scale integration of the plasma proteome with genetics and disease. Nat. Genet. 53, 1712–1721 (2021). 10.1038/s41588-021-00978-w [PubMed: 34857953]

51. Schwartzentruber J et al. Genome-wide meta-analysis, fine-mapping and integrative prioritization implicate new Alzheimer's disease risk genes. Nat. Genet. 53, 392–402 (2021). 10.1038/s41588-020-00776-w [PubMed: 33589840]

52. Xiang X et al. Microglial activation states drive glucose uptake and FDG-PET alterations in neurodegenerative diseases. Sci Transl Med 13, eabe5640 (2021). 10.1126/scitranslmed.abe5640 [PubMed: 34644146]

53. Zimmer ER, Pascoal TA, Rosa-Neto P, Nordberg A & Pellerin L Comment on "Microglial activation states drive glucose uptake and FDG-PET alterations in neurodegenerative diseases". Sci Transl Med 14, eabm8302 (2022). 10.1126/scitranslmed.abm8302 [PubMed: 36001681]

Methods-Only References

54. Weber B et al. TREM-1 deficiency can attenuate disease severity without affecting pathogen clearance. PLoS Pathog 10, e1003900 (2014). 10.1371/journal.ppat.1003900 [PubMed: 24453980]

55. Oakley H et al. Intraneuronal beta-amyloid aggregates, neurodegeneration, and neuron loss in transgenic mice with five familial Alzheimer's disease mutations: potential factors in amyloid plaque formation. J. Neurosci. 26, 10129–10140 (2006). 10.1523/JNEUROSCI.1202-06.2006 [PubMed: 17021169]

56. Yousef H et al. Aged blood impairs hippocampal neural precursor activity and activates microglia via brain endothelial cell VCAM1. Nat. Med. 25, 988–1000 (2019). 10.1038/s41591-019-0440-4 [PubMed: 31086348]

57. Wang L et al. Peak Annotation and Verification Engine for Untargeted LC-MS Metabolomics. Anal. Chem. 91, 1838–1846 (2019). 10.1021/acs.analchem.8b03132 [PubMed: 30586294]

58. Adusumilli R & Mallick P Data Conversion with ProteoWizard msConvert. Methods Mol. Biol. 1550, 339–368 (2017). 10.1007/978-1-4939-6747-6_23 [PubMed: 28188540]

59. Clasquin MF, Melamud E & Rabinowitz JD LC-MS data processing with MAVEN: a metabolomic analysis and visualization engine. Curr Protoc Bioinformatics Chapter 14, Unit14 11 (2012). 10.1002/0471250953.bi1411s37

60. Melamud E, Vastag L & Rabinowitz JD Metabolomic analysis and visualization engine for LC-MS data. Anal. Chem. 82, 9818–9826 (2010). 10.1021/ac1021166 [PubMed: 21049934]

61. Pang Z et al. MetaboAnalyst 5.0: narrowing the gap between raw spectra and functional insights. Nucleic Acids Res 49, W388–W396 (2021). 10.1093/nar/gkab382 [PubMed: 34019663]

62. Young K & Morrison H Quantifying Microglia Morphology from Photomicrographs of Immunohistochemistry Prepared Tissue Using ImageJ. J Vis Exp (2018). 10.3791/57648

63. Chaney AM, Johnson EM, Cropper HC & James ML PET Imaging of Neuroinflammation Using [11C]DPA-713 in a Mouse Model of Ischemic Stroke. J Vis Exp (2018). 10.3791/57243

64. Casali BT & Landreth GE Aβ Extraction from Murine Brain Homogenates. Bio Protoc 6 (2016). 10.21769/BioProtoc.1787

65. Beach TG et al. Arizona Study of Aging and Neurodegenerative Disorders and Brain and Body Donation Program. Neuropathology 35, 354–389 (2015). 10.1111/neup.12189 [PubMed: 25619230]

66. Consensus recommendations for the postmortem diagnosis of Alzheimer's disease. The National Institute on Aging, and Reagan Institute Working Group on Diagnostic Criteria for the Neuropathological Assessment of Alzheimer's Disease. Neurobiol. Aging 18, S1–2 (1997). [PubMed: 9330978]

67. Braak H & Braak E Neuropathological stageing of Alzheimer-related changes. Acta Neuropathol. (Berl). 82, 239–259 (1991). [PubMed: 1759558]

68. McKeith IG et al. Diagnosis and management of dementia with Lewy bodies: third report of the DLB Consortium. Neurology 65, 1863–1872 (2005). 10.1212/01.wnl.0000187889.17253.b1 [PubMed: 16237129]

69. Dickson DW Required techniques and useful molecular markers in the neuropathologic diagnosis of neurodegenerative diseases. Acta Neuropathol 109, 14–24 (2005). 10.1007/s00401-004-0950-z [PubMed: 15645265]

70. Hemani G, Tilling K & Davey Smith G Orienting the causal relationship between imprecisely measured traits using GWAS summary data. PLoS Genet 13, e1007081 (2017). 10.1371/journal.pgen.1007081 [PubMed: 29149188]

71. Hemani G et al. The MR-Base platform supports systematic causal inference across the human phenome. Elife 7 (2018). 10.7554/eLife.34408

72. Liu Q et al. PGE2 signaling via the neuronal EP2 receptor increases injury in a model of cerebral ischemia. Proc. Natl. Acad. Sci. U. S. A. 116, 10019–10024 (2019). 10.1073/pnas.1818544116 [PubMed: 31036664]

73. Iweka CA et al. Myeloid deficiency of the intrinsic clock protein BMAL1 accelerates cognitive aging by disrupting microglial synaptic pruning. J Neuroinflammation 20, 48 (2023). 10.1186/s12974-023-02727-8 [PubMed: 36829230]

74. Blacher E et al. Aging disrupts circadian gene regulation and function in macrophages. Nat Immunol 23, 229–236 (2022). 10.1038/s41590-021-01083-0 [PubMed: 34949832]

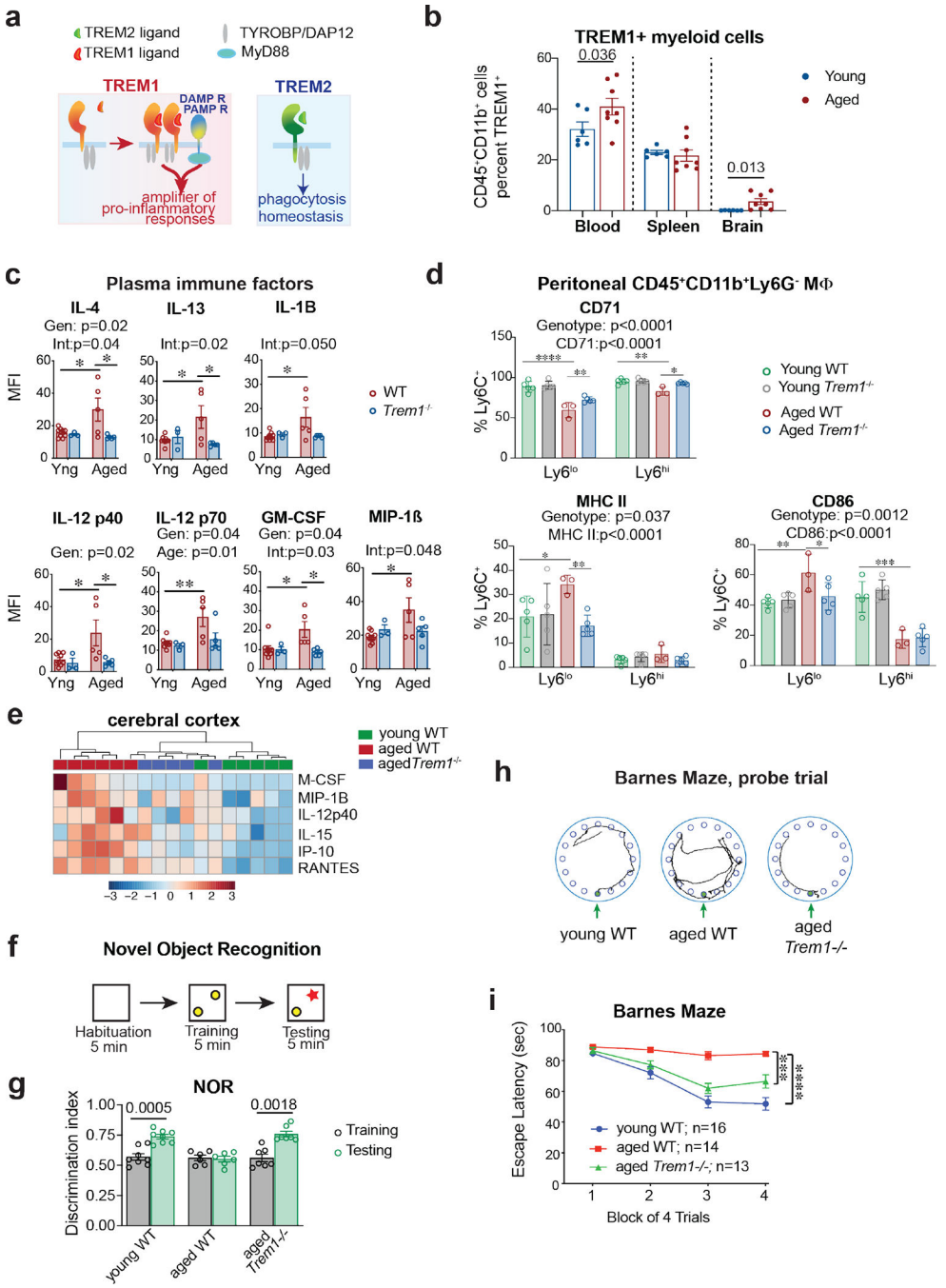

Figure 1. TREM1 deficiency prevents age-associated inflammation and memory decline

Data are represented as mean +/− SEM.

a. TREM1 expression on myeloid cells is low under basal conditions, however with stimulation by PAMPs or DAMPs, TREM1 synergizes with innate immune receptors to amplify the pro-inflammatory response. Its functional counterpart TREM2 promotes phagocytosis and cell survival.

b. Percent TREM1 surface expression across blood, spleen and brain $CD45^{+}CD11b^{+}$ myeloid cells in young (3 mo) and aged (13–17 mo) male mice. Student's t-test, one-tailed (n=6–8 mice per group as shown).

c. Multi-analyte quantification of plasma immune factors from young (3 mo) and aged (18.5 mo) WT and *Trem1−/−* male mice. Two-way ANOVA, effect sizes shown for genotype (Gen) and interaction (Int); post-hoc Tukey comparisons: * $P < 0.05$ (n=3–9 male mice/group as shown).

d. Flow cytometric analysis of anti-inflammatory CD71 and pro-inflammatory MHCII and CD86 in $Ly6C^{Hi}$ and $Ly6C^{Lo}$ peritoneal MΦ from young 2 mo WT and aged 22–23 mo WT and *Trem1*$^{-/-}$ male mice. Two-way ANOVA, effect sizes shown for genotype and marker; post-hoc Tukey comparisons: *$P < 0.05$, **$P < 0.01$, ***$P < 0.001$, ****$P < 0.0001$ (n=3–5 male mice/group as shown).

e. Unsupervised hierarchical clustering of significantly regulated immune factors by one-way ANOVA in cortical lysates from young wild-type (2 mo) and aged WT (25 mo) and *Trem1*$^{-/-}$ (23.5 mo) male mice, (n=5–6 male mice/group as shown).

f. The Novel Object Recognition (NOR) task with habituation to testing arena, training phase with exploration of two identical objects and testing phase where object is replaced with a novel object.

g. Discrimination index for the NOR task for young WT (5 mo), aged WT (18 mo) and aged *Trem1−/−* (18 mo) mice; paired two tailed t-test (n = 6–8 male and female mice/group as shown).

h. Representative movement tracings for final training trial of the Barnes maze. Escape hole is labelled with green arrow.

i. Escape latency on the Barnes maze. 2-way repeated measures ANOVA: interaction between training and genotype ($F_{(6,120)} = 7.38$, $P < 0.0001$); Tukey's post hoc: ***$P < 0.001$, ****$P < 0.0001$ (n= 16 young WT, 14 aged WT, and 13 aged *Trem1−/−* male and female mice/group).

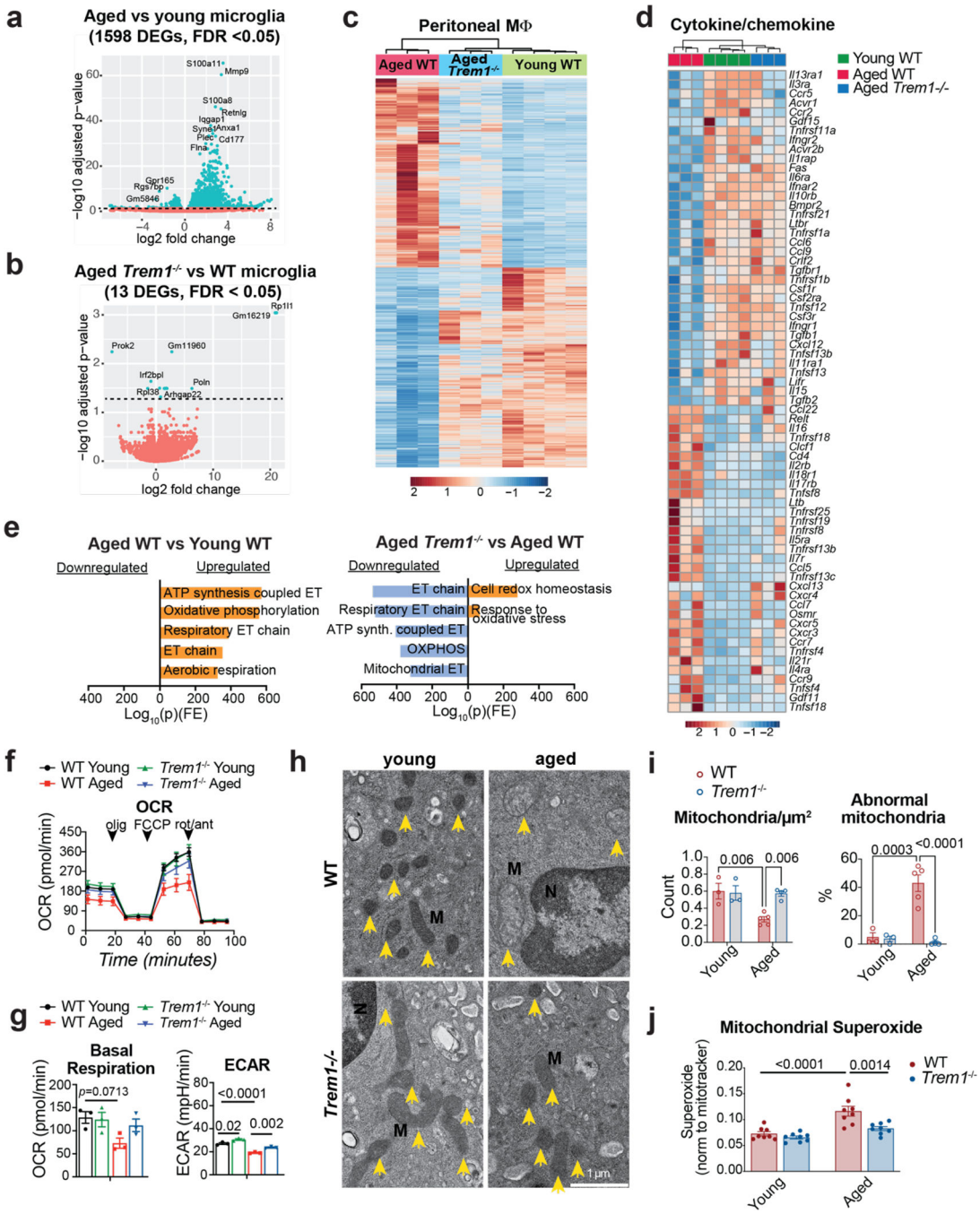

Figure 2. TREM1 is activated in peripheral macrophages in aging.

Data are mean ± s.e.m. unless otherwise indicated.

a. Volcano plot of DEGs from aged (18 – 20 mo) vs young (3 mo) CD45^{low}CD11b^{+} microglia with $-\log_{10}(P) > 1$ after FDR adjustment and $\log_2$ fold change > 1. n=3 samples/age (each sample pooled from 2 male mice).

b. Volcano plot of DEGs from aged *Trem1−/−* vs aged WT microglia with $-\log_{10}(P) > 1.25$ after FDR and $\log_2$ fold change > 1. n=3 samples/genotype (each sample pooled from 2 male mice).

c. Unsupervised hierarchical clustering of DEGs from mouse peritoneal MΦ from young WT (2 mo), aged WT (25 mo) and aged *Trem1*$^{-/-}$ (25 mo) mice. Scale represents z-score values of FPKM (n=3–4 male mice/group).

d. Unsupervised hierarchical clustering of cytokine and chemokines DEGs ($q < 0.05$). Scale represents z-score values from FPKM (n=3–4 mice/group).

e. Pathway enrichment analysis of DEGs in the Mouse MitoCarta3.0 gene list. Scale represents Log(p) × fold enrichment (FE).

f. Representative oxygen consumption rate (OCR) traces with SeaHorse for young (4.5 mo) and aged (22–23 mo) wild-type (WT) and *Trem1*$^{-/-}$ peritoneal MΦ (n= 5 male mice/group). Arrowheads indicate application of electron transport-chain inhibitors. Abbreviations: olig: oligomycin, FCCP: carbonyl cyanide-4 (trifluoromethoxy) phenylhydrazone, rot/ant: rotenone/antimycin A (n=5 male mice/group).

g. Quantification of basal respiration and glycolysis (extracellular acidification rate, or ECAR) for young (4.5 mo) and aged (22–23 mo) WT and *Trem1*$^{-/-}$ peritoneal MΦ. Two-way ANOVA, Tukey's multiple comparisons shown; effect of age, $P<0.0001$ and genotype, $P=0.0001$ (OCR, n=3 male mice/group; ECAR, n=3 male mice/group).

h. Transmission electron microscopy (TEM) images of young (4.5 mo) and aged (24–26 mo) *Trem1*$^{-/-}$ and WT peritoneal MΦ. Yellow arrows indicate mitochondria. Abbreviations: M: mitochondrion; N: nucleus. Scale = 1 μm.

i. Numbers of MΦ mitochondria and percent abnormal mitochondria from (h). Two-way ANOVA, Tukey's multiple comparisons shown; effect of age, $P=0.0021$; genotype, $P=0.0005$; interaction, $P=0.0008$ (n= 3–5 male mice/group).

j. Mitochondrial superoxide production in peritoneal MΦ, normalized to MitoTracker signal, in young (4 mo) and aged (20 mo) male WT and *Trem1*$^{-/-}$ mice, n=8 mice/group. Two-way ANOVA with Tukey's multiple comparisons test; effect of age, $P<0.0001$; genotype, $P=0.0012$; interaction, $P=0.0289$.

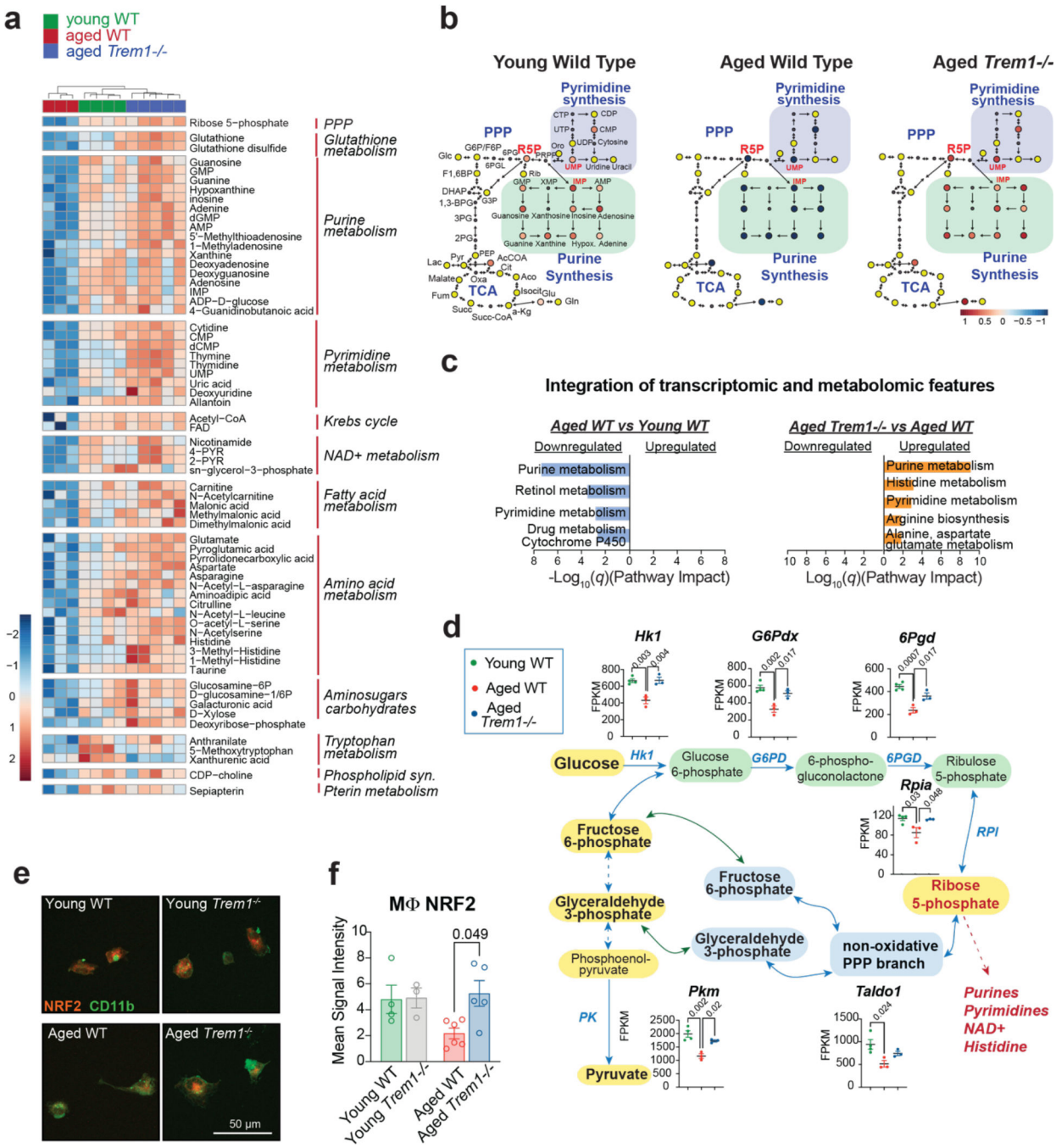

Figure 3. TREM1 suppresses pentose phosphate pathway (PPP) generation of Ribose 5P and purine/pyrimidine synthesis in aged macrophages

a. Unsupervised hierarchical clustering of significantly regulated metabolites from peritoneal MΦ isolated from young WT (2 mo), aged WT (25 mo) and aged *Trem1*$^{-/-}$ (25 mo) male mice. TREM1-deficient MΦ cluster with young WT MΦ. Data were analyzed and clustered using MetaboAnalyst 5.0; n=3–5 male mice per group as shown.

b. Metabolic pathway map of glycolysis, pentose phosphate pathway (PPP), TCA cycle, and purine and pyrimidine synthesis demonstrates decrease of Ribose 5-Phosphate (R5P), the precursor of purine and pyrimidine synthesis, in aged WT MΦ that is restored to young

WT levels with *Trem1* deletion. Colored circles represent z-scored fold change levels for significantly modified metabolites. Yellow circles indicate no significant difference. Small gray circles indicate metabolites that were not measured.

c. Integration of transcriptomic and metabolomic features demonstrates enrichment in purine and pyrimidine metabolism. Included in the joint pathway analysis were differentially regulated metabolites ($q < 0.05$) and the highest regulated DEGs (q-values < 0.05 and Log2FC > +/−2) and fold change for each feature. No pathways were enriched in the comparison between aged *Trem1*$^{-/-}$ and young WT. Data were analyzed using the Joint Pathway Analysis function in MetaboAnalyst 5.0.

d. Glycolysis and PPP enzymes (blue) with FPKM quantification. 1-way ANOVA with Tukey's multiple comparisons shown (n=3–4 male mice/group as shown). Abbreviations: 6PGD: 6-phosphogluconate dehydrogenase; G6PD: glucose-6-phosphate dehydrogenase; HK1: hexokinase-1, PK: pyruvate kinase; RPI: ribose-5-phosphate isomerase. Enzymes *G6pdx*, *6Pgd*, *Rpia*, *Taldo1* and *Pkm* are known NRF2 target genes. Data are shown as mean ± s.e.m.

e. Immunofluorescent localization of NRF2 in CD11b^{+} peritoneal MΦ isolated from (4.5 mo) and aged (24–26 mo) WT and *Trem1*$^{-/-}$ male mice.

f. Quantification of total NRF2 levels in MΦ from (e). 3–5 confocal images were processed per cell using ImageJ. 2-way ANOVA, Tukey's multiple comparisons test shown (n=3–6 male mice/group as shown). Data are shown as mean ± s.e.m.

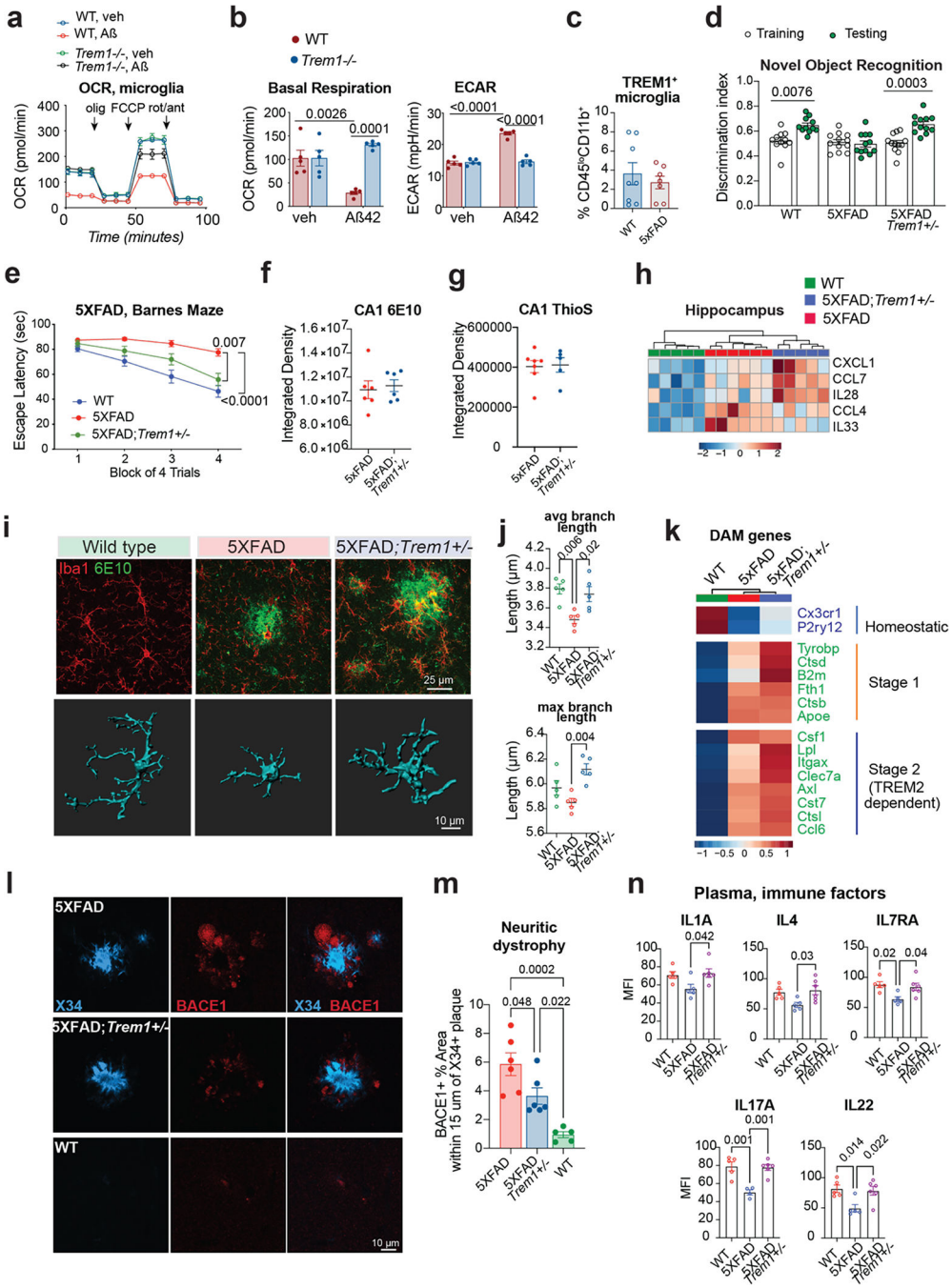

Figure 4. TREM1 deficiency preserves hippocampal function in 5XFAD mice

Data are shown as mean ± s.e.m.

a. OCR traces from postnatal mouse microglia from WT and *Trem1*$^{-/-}$ mice stimulated with vehicle or Aß$_{42}$ oligomers (100 nM) for 20 hours (n=5 wells per genotype/condition).

b. Quantification of basal respiration and glycolysis (ECAR). Two-way ANOVA with Tukey's multiple comparisons; for basal respiration, effect of genotype and interaction, P=0.0006; for ECAR, effect of genotype, Aß, and interaction, P<0.0001 (n=5 wells per genotype/condition).

c. Percent TREM1^{+}CD45^{lo}CD11b^{+}microglia in WT vs 5XFAD mice (n=6–8 male and female mice/group as shown, 13–17 mo)

d. Novel Object Recognition (NOR) of 6–7 mo WT, 5XFAD and 5XFAD; *Trem1*$^{+/-}$ mice. Training (clear circles) and testing (green circles) discrimination index differences were assessed with paired *t*-tests. Discrimination index of 0.5 indicates chance preference (n=11–12 male and female mice/condition).

e. Escape latency of 5XFAD cohorts on the Barnes maze. 2-way repeated measures (RM) ANOVA with Tukey's multiple comparisons. Interaction between training and mouse genotype [$F_{(6,90)} = 4.14$, $P < 0.001$)] (n=11 WT, n=12 5XFAD, n=10 5XFAD; *Trem1*$^{+/-}$ male and female mice/group).

f. Mean integrated density of 6E10 signal from hippocampal CA1 of 9–10 mo 5XFAD and 5xFAD; *Trem1*$^{+/-}$ mice (n=6 female mice/group).

g. Mean integrated density of ThioS signal, a marker of fibrillar amyloid, from CA1 of 9–10 mo 5XFAD and 5xFAD; *Trem1*$^{+/-}$ mice (n=5–7 female mice/group).

h. Unsupervised hierarchical clustering of significantly regulated immune proteins in hippocampus from 9–10 mo WT, 5XFAD, and 5XFAD; *Trem1*$^{+/-}$ mice, one-way ANOVA (n=5–6 female mice/group).

i. Immunofluorescent images of Iba1+ microglia and 6E10 staining of amyloid in CA1 of 9–10 mo WT, 5XFAD, and 5XFAD; *Trem1*$^{+/-}$ female mice and 3-dimensional rendering of representative microglia. Scale bar is 25μm (top row) and 10 μm (bottom row).

j. Quantification of average microglial branch length and maximum branch length. One-way ANOVA with Tukey's multiple comparison (n=5 female mice/group).

k. Heatmap depicting group means of significantly regulated (one-way ANOVA) DAM signature genes. Microglia samples were pooled from two 6–7 mo male mice (n=3 samples per genotype). Scale represents z-score values from FPKM.

l. Neuritic dystrophy visualized with anti-BACE1 immunostaining at X34+ amyloid plaques in WT, 5XFAD, and 5XFAD; *Trem1*$^{+/-}$ 9–10 mo female mice; scale bar=10 μm

m. Quantification of BACE1-positive percent area around amyloid plaques. One-way ANOVA with Tukey's multiple comparisons (n= 5–6 female mice/group).

n. Quantification of plasma immune factors in WT, 5XFAD, and 5XFAD; *Trem1*$^{+/-}$ 9–10 mo mice. One-way ANOVA with Tukey's multiple comparisons (n= 4–6 female mice/group).

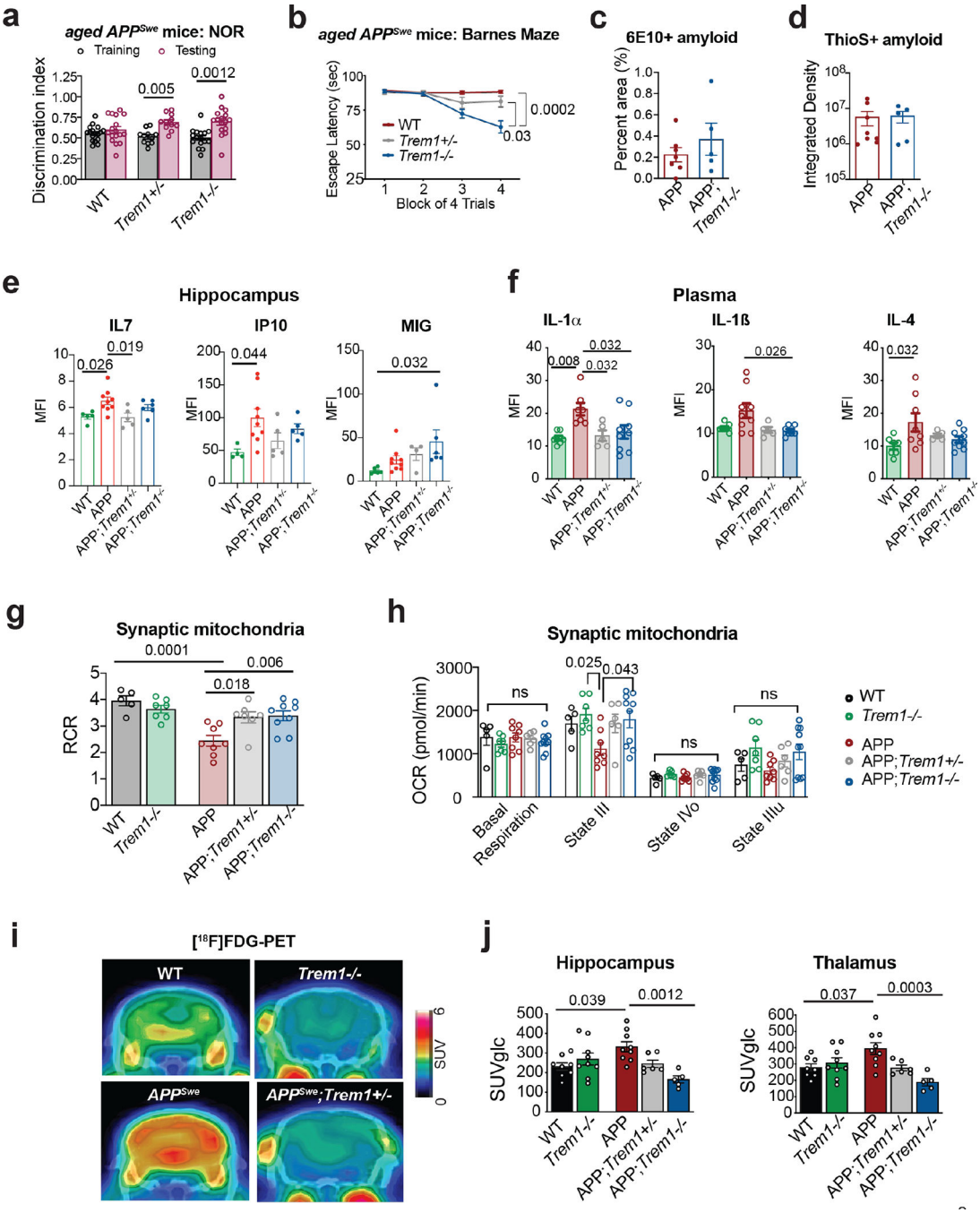

Figure 5. M1 deficiency preserves hippocampal spatial memory and brain glucose uptake in *APP*^{Swe} mice

Data are shown as mean ± s.e.m.

a. Discrimination index during the NOR task for aged (18–21 mo) *APP*^{Swe}, *APP*^{Swe}/*Trem1*$^{+/-}$ and *APP*^{Swe}/*Trem1*$^{-/-}$ mice; paired t-test of Training vs. Testing (n=11–17 male and female mice/group as shown).

b. Escape latency of *APP*^{Swe} cohorts in the Barnes maze. 2-way repeated measures ANOVA with Tukey's multiple comparisons. Interaction between training and mouse genotype

[$F_{(6,132)} = 12.24$, $P < 0.0001$)] (n=17 APP^{Swe}, 14 $APP^{Swe}/Trem1^{+/-}$ and 16 $APP^{Swe}/Trem1^{-/-}$ male and female mice/group).

c. Percent area positive for 6E10 in hippocampus of 18–21 mo APP^{Swe} and $APP^{Swe};Trem1^{-/-}$ mice. Student's two tailed t-test (n=5–7 male/female mice/group as shown).

d. Average integrated density for $ThioS^{+}$ signal in hippocampus of 18–21 mo APP^{Swe} and $APP^{Swe};Trem1^{-/-}$ mice. Student's two tailed t-test, n=5–8 male/female mice/group as shown.

e. Hippocampal immune factors in 20–23 mo in WT, APP^{Swe}, $APP^{Swe}/Trem1^{+/-}$ and $APP^{Swe}/Trem1^{-/-}$ mice. One-way ANOVA with Tukey's multiple comparisons (n=4–9 female mice/group as shown).

f. Plasma cytokines in 20–23 mo in WT, APP^{Swe}, $APP^{Swe}/Trem1+/-$ and $APP^{Swe}/Trem1-/-$ mice. One-way ANOVA with Tukey's multiple comparisons (n=4–9 female mice/group as shown).

g. Respiratory control ratio (RCR) in synaptic mitochondria fractions from 18–24 mo mouse brain. High RCR indicates mitochondria with a high capacity for substrate oxidation and ATP turnover and a low proton leak. One-way ANOVA with Tukey's multiple comparisons (n=5–9 male mice/group as shown).

h. Synaptic mitochondria OCR (pmol/min) calculated basally and for state III, state IVo, and state IIIu in 18–24 mo WT, APP^{Swe} and in $APP^{Swe};Trem1^{-/-}$ mice. State III reflects maximal ADP-stimulated respiration and State IV reflects the return to a basal state of respiration after addition of ATP synthase inhibitor oligomycin. One-way ANOVA with Tukey's multiple comparisons (n=5–9 male mice/group as shown).

i. Representative coronal brain [^{18}F]FDG-PET/CT images of cerebral glucose metabolism in 17–19 mo female mice. SUV: standardized uptake values. Static 20 min PET images were acquired at 75–95 min following [^{18}F]FDG injection.

j. Quantification of [^{18}F]FDG-PET signal in hippocampus and thalamus. SUVs were normalized to individual blood glucose concentrations. One-way ANOVA with Tukey's multiple comparisons (n=5–9 female mice/group).

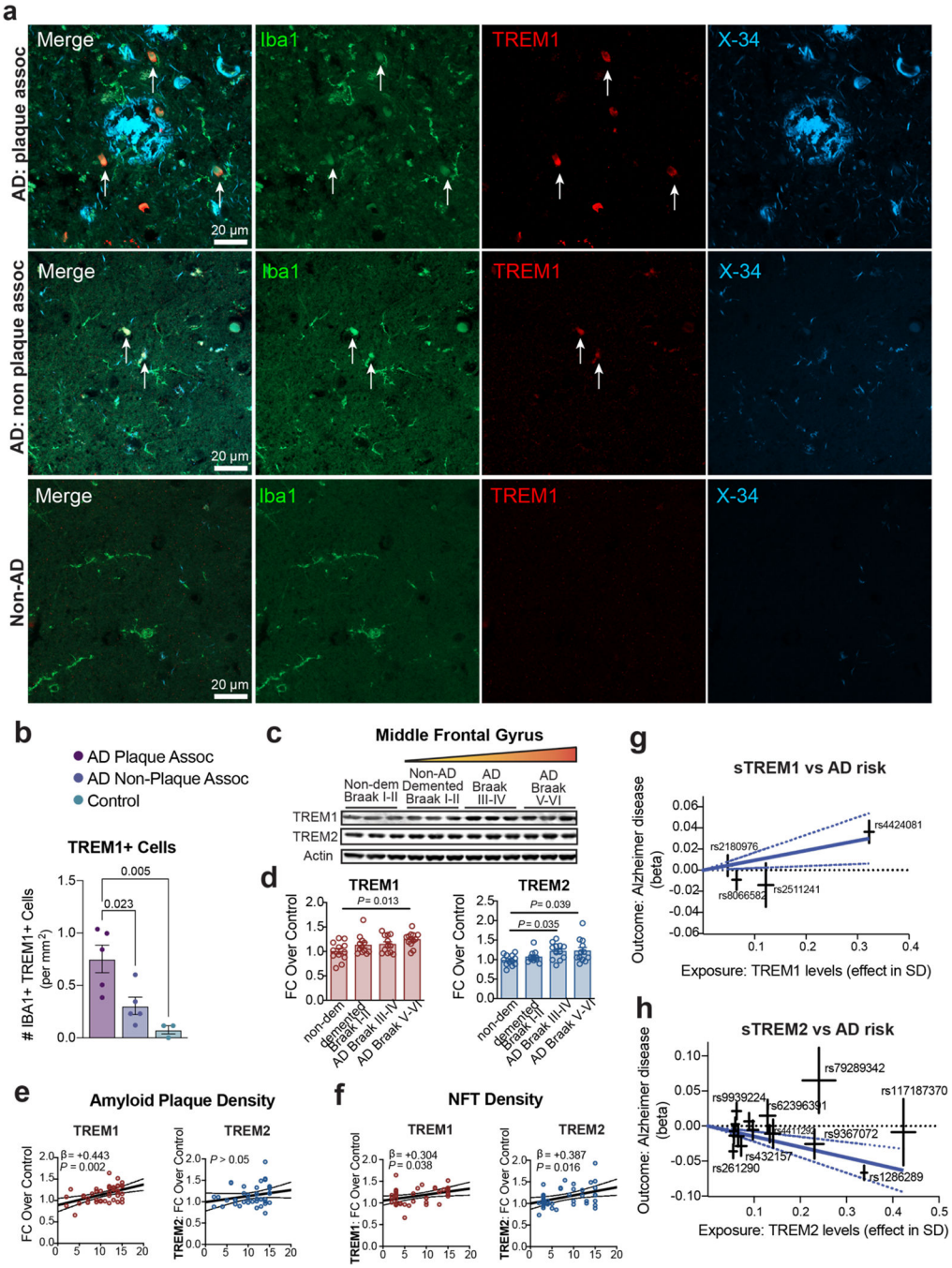

Figure 6. Myeloid TREM1 expression positively associates with increasing AD pathology.

Data are shown as mean ± s.e.m. unless otherwise indicated.

a. Immunofluorescent staining of human frontal cortex for TREM1 (red), Iba1 (green), and X-34 (blue). TREM1+/Iba1+ cells are defined as plaque associated (within 15 µm of an X-34+ amyloid plaque) or non-plaque associated. Scale bar = 20 µm. White arrows indicate colocalization of Iba1 and TREM1.

b. Quantification of TREM1+/Iba1+ plaque-associated and non-plaque-associated cells. One-way ANOVA with Tukey's multiple comparisons. n=5 AD donors and n=3 Control donors.

c. Immunoblot of TREM1 and TREM2 in middle frontal gyrus across clinicopathological diagnoses (n=11–12 donors/group).

d. Quantification of TREM1 and TREM2 protein normalized to ß-actin and expressed as fold-change over non-demented control. ANCOVA with Tukey's multiple comparisons. Age and sex were included as covariates (n=11–12 donors/group).

e. Linear regression analyses between amyloid plaque and neurofibrillary tangle (NFT) density and TREM1 (left plot) and TREM2 (right plot) levels from quantitative immunoblotting. Model was adjusted for age and sex. Plotted are the 95% confidence bands of the best-fit line from the linear regression. The standardized regression coefficients (ß) and P-values from the linear model are shown. n=43 donors (amyloid plaque density vs TREM1) and n=42 donors (amyloid plaque density vs TREM2).

f. Linear regression analyses between neurofibrillary tangle (NFT) density and TREM1 (left plot) or TREM2 (right plot) levels from quantitative immunoblotting; n=41 donors (NFT density vs TREM1) and n=40 donors (NFT density vs TREM2).

g. Mendelian Randomization (MR) analysis of relationship between plasma levels of soluble TREM1 (sTREM1; exposure) and Alzheimer's disease risk (outcome). Blue lines are estimated MR-inverse variance weighted effects, and dashed lines indicate the 95% confidence interval for MR effects. Increased plasma sTREM1 level was associated with increased AD risk (β = +0.0929, [95% CI = 0.019 to 0.166] $P = 0.013$).

h. Mendelian Randomization (MR) analysis showing relationship between plasma levels of soluble sTREM2 (as exposure) and Alzheimer's disease risk (outcome). Increased plasma sTREM2 level was associated with decreased AD risk (β = −0.15 [95% CI = −0.223 to −0.077] $P = 5.61\times10^{-05}$).